OPTIMIZED TARGETING IN DEEP BRAIN STIMULATION FOR MOVEMENT DISORDERS

by

Layla Houshmand

A dissertation submitted in partial fulfillment
of the requirements for the degree of
Doctor of Philosophy
(Biomedical Engineering)
in the University of Michigan
2015

Doctoral Committee:

Assistant Professor Parag G. Patil, Chair
Assistant Professor Cynthia A. Chestek
Professor Cameron C. McIntyre, Case Western Reserve University
Assistant Professor William C. Stacey
Professor Euisik P. Yoon

Acknowledgements

My graduate school experience far exceeded my expectations thanks to the mentorship and friendship of so many people. I feel extremely lucky to have been in Ann Arbor with the people I've met and worked with over the past five years.

First and foremost, I'd like to thank my adviser, Dr. Parag Patil. I am very fortunate to have become his graduate student. Dr. Patil always trusted me and made me believe in myself, and I don't think anybody else could have convinced me to be as ambitious as he did. He taught me so much about how to solve seemingly insurmountable problems and staying sane in the process. I will carry those lessons with me for the rest of my life.

I'd like to thank my committee members, Dr. Cynthia Chestek, Dr. William Stacey, Dr. Cameron McIntyre, and Dr. Euisik Yoon for many helpful discussions and their guidance along the way.

I'd like to acknowledge my funding sources, the U.S. Department of Education's Graduate Assistance in Areas of National Need (GAANN) Fellowship and the Coulter Foundation, for supporting me throughout my research.

I would not have made it through several roadblocks without help from many generous people. Dr. Ashu Chaturvedi and Angela Noecker at Case Western

Reserve University were instrumental in getting me started on my project, and I am so grateful for their instruction and patience. Ayla Khan, Dr. Darrell Swenson, and Jess Tate from the University of Utah's Scientific Computing Institute got me through a significant technical hurdle that made most of my work possible. AnalyzeDirect's technical support staff—Beth Adams, Aimee Rasmussen, and Michael Philcock—helped me almost weekly.

I'd like to thank the BME department, especially Maria Steele and Jane MacKie, for always advocating for students and making sure we all stay afloat. Dr. Aileen Huang-Saad and Dr. Brian J. Love deserve recognition for helping me find the right lab—thank you!

I am grateful for wonderful labmates— Sunjay Dodani, Charles Lu, Karlo Malaga, Melissa Wright, Karen Cummings, Kelly Lupo, Vedant Ram, and Ari Lax—who helped so much with my project and were just some of the nicest people to be around in our small office. Thank you to Marti Cotner and Heidi Zayan for always making the lab run smoothly! I will miss our Tuesday morning breakfasts.

My friends in graduate school have been some of the best people I've ever met, and I am so sad that we won't be in the same city. Our adventures took us abroad and through a few obstacle courses. My two closest friends in graduate school, Julia Kline and Marina Vigen, were my rocks in Ann Arbor. I am supremely thankful to call you both my friends, and I hope we always stay that way. Thank you to Jeremy Holzwarth, Barry Belmont, Lesli Kiedrowski, Patrick Ingram, Joshua White, Alex Emly, Joseph Labuz, David Lai, Karen Schroeder, Paras Patel, Melanie Gupte, Jake Ceccarelli, Matt LaVelle, Michael Cappo, Brandon Bruhn,

and Dave Skoog for always being up for some adventure and for being consistently great cooks for potlucks.

In 2012, I got side-tracked by a legal scuffle within the university that led me to meet some great people who I'd like to thank for fighting the good fight: Patrick Wright, Stephen Raiman, Anna Belak, Adam Duzik, Paul Giuliano. I'm proud of what we accomplished.

My parents, Ali and Farah, sacrificed so much in their lives to make mine possible. I will always be grateful to them for being so supportive and loving and always putting everything in perspective. Thank you to my brother Kasra for supporting me when it mattered. To my significant other, Jolyon: thank you for putting up with four years of flying between cities for me. Whatever I did to deserve you could not have possibly been enough!

Table of Contents

List of Figures

List of Tables

Abstract

Deep brain stimulation (DBS) is the dominant surgical therapy for medically-refractory Parkinson's Disease (PD) and Essential Tremor (ET). Despite its widespread use and success in treating the physical symptoms of many movement disorders, the mechanism of DBS is not understood, and optimal targeting protocols are yet to be determined. The success of the surgery is highly dependent upon proper placement of the electrode in the brain. However, the anatomical targets for PD and ET DBS—the subthalamic nucleus (STN) and ventral intermediate (Vim) nucleus of the thalamus, respectively—are not visible on conventional magnetic resonance imaging. Neurosurgeons typically locate these structures using atlas-based indirect targeting methods. Due to the imprecision of these techniques, multiple passes are required during surgery to find the appropriate structure(s), increasing the risk of intracranial hemorrhage. The purpose of this work was to optimize targeting in DBS for PD and ET.

In our first study, we evaluated the most common indirect STN targeting methods with our validated 3-Tesla MRI protocol optimized for STN visualization. We calculated the indirect targets as prescribed by midcommissural point-based (MCP) and red nucleus-based (RN) methods, and compared those coordinates to the position of the STN. We found that RN-based targeting is statistically superior to

MCP-based targeting and should be routinely used in the absence of direct STN visualization.

In our next study, we investigated the volume of tissue activated (VTA) in thalamic Vim DBS. First, we developed a k-means clustering algorithm that operates on diffusion tensor imaging data to semi-automatically segment the thalamus into its functionally-distinct nuclei. We segmented individual patient thalami and an atlas thalamus in an existing VTA model, and created an individualized VTA model by utilizing each patient's own anatomy and tissue conductivity. We measured stimulation overlaps with relevant nuclei for clinically efficacious stimulation settings. There was a statistical trend towards greater precision in individualized modeling's electrode placement with respect to the Vim nucleus, and our preliminary results indicated that individualized VTA modeling may better explain tremor control than existing atlas-based VTA modeling.

Finally, utilizing the methods from our prior study, we investigated the ability of atlas-based and individualized VTA modeling methods to explain common side effects (sustained sensory paresthesias and dysarthria) from thalamic DBS. We found that only individualized VTA modeling can predict dysarthria, thus justifying its use over atlas-based modeling.

The results of this work advance the understanding of proper DBS targeting for movement disorders, and our VTA modeling system represents the most individualized approach for ET DBS surgical planning. Optimized DBS targeting improves surgical safety and overall surgical outcome.

Chapter 1

Introduction

Deep brain stimulation (DBS) is a highly effective surgical therapy for the reduction of the physical symptoms of medically-refractory Parkinson's Disease (PD), Essential Tremor (ET), and other movement disorders [1]. DBS evolved out of a need for a reversible alternative to ablative brain surgery. Despite the effectiveness of DBS, the mechanism of action is not understood; it is theorized that DBS activates the regions of the brain that it stimulates via direct axonal stimulation [2, 3], overriding any erroneous, disease-producing neural behavior [2, 4] to suppress tremor and other symptoms. The clinical efficacy of DBS surgery is highly dependent on proper placement of the DBS electrode, as small differences in stimulation location have a dramatic impact on clinical outcome [5, 6].

Neurosurgeons face challenges in proper targeting of anatomical structures associated with PD and ET. The anatomical targets for PD and ET DBS—the subthalamic nucleus (STN) and ventral intermediate (Vim) nucleus of the thalamus, respectively—are not visible on conventional (1.5T) magnetic resonance imaging (MRI) [7, 8]. Neurosurgeons typically locate these structures using a combination of atlas-based indirect targeting methods and intraoperative microelectrode recordings [9]. Due to the imprecision of these techniques, multiple

passes are required during surgery to find the appropriate structure(s), increasing the risk of intracranial hemorrhage [6, 10].

1.1 Aims

In this dissertation, we propose optimized targeting techniques for PD and ET DBS. For PD DBS, we investigate indirect targeting methods with a purely anatomical approach. For ET DBS, we employ a more complex analysis with volume of tissue activated (VTA) modeling and thalamic segmentation to investigate tremor control and side effects.

In our first aim, we apply a validated 3T MRI protocol optimized for STN visualization to in determining the accuracy and precision of midcommissural point-based (MCP) and red nucleus-based (RN) indirect STN targeting methods. We hypothesize that RN-based targeting, though less commonly utilized, is actually more accurate and precise than MCP-based targeting and should be routinely used in the absence of direct STN visualization.

Next, we present methodology for individualized VTA modeling for thalamic DBS for ET. We propose a k-means clustering algorithm that operates on diffusion tensor imaging data to semi-automatically segment the thalamus into its functionally-distinct nuclei, allowing for thalamic Vim targeting. Using the results of segmentation, we calculate individualized and atlas-based VTAs of DBS stimulation settings eliciting optimal tremor control. We hypothesize that individualized segmentations and VTA modeling result in: 1) more precise electrode placement with respect to the Vim nucleus and 2) VTAs that lie primarily

within the motor thalamus during optimal tremor control, when compared to atlas-based VTA modeling.

Lastly, utilizing the methods from the prior study, we investigate the ability of atlas-based and individualized VTA modeling methods to explain common side effects (sustained sensory paresthesias and dysarthria) from thalamic DBS. We hypothesize that individualized VTA modeling will better predict the incidence of common side effects in thalamic DBS, justifying its use over atlas-based VTA modeling.

1.2 Background

1.2.1 Movement Disorders: ET and PD

ET is the most common movement disorder among adults and is also considered to be one of the most common adult neurological disorders [11-14]. Despite its prevalence, the etiology of ET is poorly understood [15]. ET is characterized by a 5-10 Hz kinetic and sometimes postural tremor [16]. According to one clinical study, approximately 15% of ET patients were unable to work due to the severity of their tremor [12, 17]. Several studies have demonstrated that high-frequency DBS of the ventral intermediate (VIM) nucleus of the thalamus is both safe and effective (83% reduction) in controlling contralateral kinetic and postural tremor in ET [18-22]. The most common side effects from ET DBS are sensory paresthesias, dysarthria, and motor contractions [21, 23]**.** When adjusting stimulation settings, patients typically experience transient paresthesias or other side effects that dissipate quickly [23]. However, in some stimulation settings, the side effects become intolerable for the patient. DBS side effects may result from improper

lead placement, contact selection, or stimulation settings (voltage, frequency, pulse width).

By contrast, PD is characterized by a 4-6 Hz resting tremor [17], and its mechanism is well understood. In PD, the death of dopaminergic neurons in the substantia nigra pars compacta (SNpc) [24] causes a dis-regulation in the basal ganglia that results in resting tremor, bradykinesia, and rigidity. In its healthy state, the SNpc operates on the striatum via the indirect (D2 receptors) and direct (D1 receptors) pathways. In the indirect pathway, the SNpc inhibits the striatal neurons that inhibit the globus pallidus externus (GPe), which in turn inhibits the STN. The STN then excites the globus pallidus internus (GPi), which stimulates the motor thalamus, providing additional stimulation to the cortex. In the direct pathway, the SNpc excites striatal neurons that inhibit the GPi, which in turn inhibits the motor thalamus and thus the stimulation to the cortex, modulating the effect of the indirect pathway. In PD, lack of activity from the SNpc causes excessive activity in the STN and a lack of activity in the GPi, ultimately resulting in excessive inhibition of the thalamus and a lack of stimulation of the cortex [25, 26].

1.2.2 DBS Targeting for ET and PD

Due to the inability to visualize thalamic nuclei with MRI [8], the Vim nucleus is commonly targeted using an indirect approach derived from the Schaltenbrand-Wahren atlas. The distal tip of the electrode is placed at the following coordinates at an anterior angle of 60-80° and a lateral angle parallel to the midsagittal plane. VIM distal tip indirect target, based on SW atlas [27]

	Vim Target (Distal Tip)
X	11.5 mm lateral + 0.5*(3rd ventricle width)
Y	Anterior to PC by 20% of AC-PC length
Z	0

Table 1-1. Indirect targeting of the Vim for DBS surgery. The target is derived from the Schaltenbrand-Wahren Atlas and represents the target coordinates for the distal tip of the DBS electrode. (UMich protocol)

Though there are a number of reports of direct visualization of the Vim [28-30], none of these methods appear more reliable than indirect targeting for routine application.

Conversely, the STN can be visualized for direct targeting with high-field MRI [31]; however, at institutions where such imaging is unavailable, indirect targeting methods derived from the Schaltenbrand-Wahren atlas are utilized. The two most common methods are summarized in Table 1-1.

	MCP-Based Targeting	RN-Based Targeting
X	12 mm lateral	3 mm lateral of lateral border
Y	3-4 mm posterior	Y-coordinate of anterior border
Z	3-5 mm inferior	2 mm inferior of superior border

Table 1-2. Indirect targeting of the STN for DBS surgery. [7, 27]

1.2.3 VTA Modeling

VTA modeling allows researchers to estimate the spatial extent of activation in the brain during DBS by accounting for underlying tissue conductivity. The VTA is an estimate of the region(s) of the brain that fires action potentials under a given set of stimulation parameters [32].To briefly describe the VTA calculation process, a Fourier FEM Solver first solves the Poisson equation to determine voltage as a function of time and space within the patient's brain tissue. The voltage solution is

dependent upon several factors, including where the electrode is placed in the brain, the patient's brain conductivity at the voxel level nearest to the electrode contacts, the stimulation settings being modeled, and the electrode-tissue interface (electrode capacitance and impedance). The VTA is defined as the region(s) for which the second spatial derivative of the extracellular potential distribution [33, 34] exceeds an axonal activation threshold derived from NEURON [35] modeling [32, 36].

Though atlas-based VTA modeling makes several simplifying assumptions regarding brain structure and tissue conductivity, it provides a mechanism for correlating patient outcomes to the anatomical regions stimulated by DBS and for determining optimal stimulation settings for clinical benefit. Frankenmolle et al. (2010) showed that an electric field model for DBS can predict DBS settings that cause fewer side effects than clinically-determined stimulation side-effects [37]. Chaturvedi et al. (2010) demonstrated that the electric field models for DBS can predict motor side-effects in PD patients [38]. There are many other published studies investigating STN stimulation for PD, [32, 36-42] however, ET DBS has yet to be modeled extensively.

The accuracy of the existing VTA model is limited by its reliance on an atlas brain; both the anatomical nuclei and tissue conductivities are derived from the Wakana et al. DT-based white matter anatomy atlas [43], which may not accurately represent the anatomy or tissue conductivity properties of many other patients. There exists an opportunity to potentially improve the accuracy and precision of VTA modeling by moving towards an individualized approach, i.e., by utilizing high-field MR and DT images to construct patient anatomy and underlying tissue

conductivity for VTA calculation. The improved methodology may be applied to an investigation of thalamic DBS for ET.

1.3 Overview

This dissertation is organized into 5 chapters. Chapter 2 is an evaluation of the accuracy and precision of the most commonly utilized indirect targeting methods for STN DBS for PD. Chapter 3 introduces a novel targeting approach for thalamic DBS, and presents some preliminary evaluation of its use in VTA modeling. Chapter 4 presents the implementation of the methods presented in Chapter 3 to investigate the VTAs of side effect inducing stimulation in thalamic DBS for ET. Chapter 5 presents the conclusions from the work presented in this dissertation and proposes future directions.

1.4 References

1. Collins, K.L., E.M. Lehmann, and P.G. Patil, *Deep brain stimulation for movement disorders.* Neurobiology of disease, 2010. **38**(3): p. 338-45.

2. Johnson, M.D., et al., *Mechanisms and targets of deep brain stimulation in movement disorders.* Neurotherapeutics, 2008. **5**(2): p. 294-308.

3. Sotiropoulos, S.N. and P.N. Steinmetz, *Assessing the direct effects of deep brain stimulation using embedded axon models.* J Neural Eng, 2007. **4**(2): p. 107-19.

4. McIntyre, C.C., et al., *Uncovering the mechanism(s) of action of deep brain stimulation: activation, inhibition, or both.* Clin Neurophysiol, 2004. **115**(6): p. 1239-48.

5. Daniluk, S., et al., *Assessment of the variability in the anatomical position and size of the subthalamic nucleus among patients with advanced Parkinson's disease using magnetic resonance imaging.* Acta Neurochirurgica, 2009. **152**(2): p. 201-210.

6. Benabid, A.L., *Deep brain stimulation for Parkinson's disease.* Curr Opin Neurobiol, 2003. **13**(6): p. 696-706.

7. Houshmand, L., et al., *Evaluating Indirect Subthalamic Nucleus Targeting with Validated 3-Tesla Magnetic Resonance Imaging.* Stereotact Funct Neurosurg, 2014. **92**(6): p. 337-345.

8. Wiegell, M.R., et al., *Automatic segmentation of thalamic nuclei from diffusion tensor magnetic resonance imaging.* Neuroimage, 2003. **19**(2 Pt 1): p. 391-401.

9. Bejjani, B.P., et al., *Bilateral subthalamic stimulation for Parkinson's disease by using three-dimensional stereotactic magnetic resonance imaging and electrophysiological guidance.* Journal of neurosurgery, 2000. **92**(4): p. 615-625.

10. Hariz, M.I. and H. Fodstad, *Do Microelectrode Techniques Increase Accuracy or Decrease Risks in Pallidotomy and Deep Brain Stimulation?* Stereotactic and functional neurosurgery, 1999. **72**(2-4): p. 157-169.

11. Louis, E.D., R. Ottman, and W.A. Hauser, *How common is the most common adult movement disorder? estimates of the prevalence of essential tremor throughout the world.* Mov Disord, 1998. **13**(1): p. 5-10.

12. Louis, E.D., *Essential tremor.* The Lancet Neurology, 2005. **4**(2): p. 100-110.

13. Kurtzke, J.F., *The current neurologic burden of illness and injury in the United States.* Neurology, 1982. **32**(11): p. 1207-14.

14. Hubble, J.P., K.L. Busenbark, and W.C. Koller, *Essential Tremor.* Clinical Neuropharmacology, 1989. **12**(6): p. 453-482.

15. Louis, E.D. and J.P. Vonsattel, *The emerging neuropathology of essential tremor.* Mov Disord, 2008. **23**(2): p. 174-82.

16. Elble, R.J., *Central mechanisms of tremor.* J Clin Neurophysiol, 1996. **13**(2): p. 133-44.

17. Deuschl, G., P. Bain, and M. Brin, *Consensus statement of the Movement Disorder Society on Tremor. Ad Hoc Scientific Committee.* Mov Disord, 1998. **13 Suppl 3**: p. 2-23.

18. Ondo, W., et al., *Unilateral thalamic deep brain stimulation for refractory essential tremor and Parkinson's disease tremor.* Neurology, 1998. **51**(4): p. 1063-9.

19. Benabid, A.L., et al., *Chronic electrical stimulation of the ventralis intermedius nucleus of the thalamus as a treatment of movement disorders.* J Neurosurg, 1996. **84**(2): p. 203-14.

20. Koller, W., et al., *High-frequency unilateral thalamic stimulation in the treatment of essential and parkinsonian tremor.* Ann Neurol, 1997. **42**(3): p. 292-9.

21. Koller, W.C., et al., *Long-term safety and efficacy of unilateral deep brain stimulation of the thalamus in essential tremor.* Mov Disord, 2001. **16**(3): p. 464-8.

22. Kumar, R., et al., *Long-term follow-up of thalamic deep brain stimulation for essential and parkinsonian tremor.* Neurology, 2003. **61**(11): p. 1601-4.

23. Marks, W.J., Jr., *Deep Brain Stimulation Management*. 2011, New York: Cambridge University Press.

24. Kleiner-Fisman, G., et al., *Subthalamic nucleus deep brain stimulation: summary and meta-analysis of outcomes.* Mov Disord, 2006. **21 Suppl 14**: p. S290-304.

25. Dauer, W. and S. Przedborski, *Parkinson's disease: mechanisms and models.* Neuron, 2003. **39**(6): p. 889-909.

26. Kravitz, A.V., et al., *Regulation of parkinsonian motor behaviors by optogenetic control of basal ganglia circuitry.* Nature, 2010. **466**(7306): p. 622-626.

27. Schaltenbrand, G., W. Wahren, and R. Hassler, *Atlas for Stereotaxy of the Human Brain*. 1977, Stuttgart: G. Thieme.

28. Yamada, K., et al., *MR imaging of ventral thalamic nuclei.* AJNR Am J Neuroradiol, 2010. **31**(4): p. 732-5.

29. Spiegelmann, R., et al., *Stereotactic targeting of the ventrointermediate nucleus of the thalamus by direct visualization with high-field MRI.* Stereotact Funct Neurosurg, 2006. **84**(1): p. 19-23.

30. Vassal, F., et al., *Direct stereotactic targeting of the ventrointermediate nucleus of the thalamus based on anatomic 1.5-T MRI mapping with a white matter attenuated inversion recovery (WAIR) sequence.* Brain stimulation, 2012. **5**(4): p. 625-33.

31. Patil, P.G., et al., *The anatomical and electrophysiological subthalamic nucleus visualized by 3-T magnetic resonance imaging.* Neurosurgery, 2012. **71**(6): p. 1089-95; discussion 1095.

32. Butson, C.R., et al., *Patient-specific analysis of the volume of tissue activated during deep brain stimulation.* Neuroimage, 2007. **34**(2): p. 661-70.

33. Rattay, F., *Analysis of Models for External Stimulation of Axons.* Biomedical Engineering, IEEE Transactions on, 1986. **BME-33**(10): p. 974-977.

34. McNeal, D.R., *Analysis of a Model for Excitation of Myelinated Nerve.* Biomedical Engineering, IEEE Transactions on, 1976. **BME-23**(4): p. 329-337.

35. Hines, M.L. and N.T. Carnevale, *The NEURON simulation environment.* Neural Comput, 1997. **9**(6): p. 1179-209.

36. Butson, C.R., et al., *Predicting the effects of deep brain stimulation with diffusion tensor based electric field models.* Med Image Comput Comput Assist Interv, 2006. **9**(Pt 2): p. 429-37.

37. Frankemolle, A.M., et al., *Reversing cognitive-motor impairments in Parkinson's disease patients using a computational modelling approach to deep brain stimulation programming.* Brain, 2010. **133**(Pt 3): p. 746-61.

38. Chaturvedi, A., et al., *Patient-specific models of deep brain stimulation: influence of field model complexity on neural activation predictions.* Brain Stimul, 2010. **3**(2): p. 65-7.

39. Miocinovic, S., et al., *Experimental and theoretical characterization of the voltage distribution generated by deep brain stimulation.* Exp Neurol, 2009. **216**(1): p. 166-76.

40. Maks, C.B., et al., *Deep brain stimulation activation volumes and their association with neurophysiological mapping and therapeutic outcomes.* J Neurol Neurosurg Psychiatry, 2009. **80**(6): p. 659-66.

41. Butson, C.R. and C.C. McIntyre, *Tissue and electrode capacitance reduce neural activation volumes during deep brain stimulation.* Clin Neurophysiol, 2005. **116**(10): p. 2490-500.

42. Butson, C.R., et al., *Probabilistic analysis of activation volumes generated during deep brain stimulation.* Neuroimage, 2011. **54**(3): p. 2096-104.

43. Wakana, S., et al., *Fiber tract-based atlas of human white matter anatomy.* Radiology, 2004. **230**(1): p. 77-87.

Chapter 2

Evaluating Subthalamic Nucleus Indirect Targeting with a Validated 3-Tesla Magnetic Resonance Imaging Protocol

Abstract

Background/Aims: Indirect targeting of the subthalamic nucleus (STN) is commonly utilized at DBS centers around the world. The superiority of either mid-commissural point (MCP)-based or red nucleus (RN)-based indirect targeting remains to be established.

Methods: The location of the STN was determined and statistically compared to MCP- and RN-based predictions in 58 STN DBS patients, using a validated 3T MRI protocol. The influence of additional neuroanatomical parameters on STN midpoint location was evaluated. Linear regression analysis was utilized to produce an optimized MCP/RN targeting model. Targeting coordinates at 1.5T were compared to results at 3T.

Results: Accuracy and precision for RN-based targeting was superior to MCP-based targeting to predict STN midpoint location for each coordinate dimension ($p < .01$ and $p < .05$, respectively). RN-based targeting was statistically equivalent to

an optimized regression-based targeting strategy incorporating multiple neuroanatomical parameters, including third-ventricular width and overall brain size. RN-based targeting at 1.5T yielded equivalent coordinates to targeting at 3T.

Conclusions: RN-based targeting is statistically superior to MCP-based STN targeting, and accommodates broad variations in neuroanatomical parameters. Neurosurgeons utilizing indirect targeting of the STN may consider favoring RN-based over MCP-based indirect targeting methods.

Abbreviations: **STN**, subthalamic nucleus; **SN**, substantia nigra; **MCP**, mid-commissural point; **RN**, red nucleus; **PD**, Parkinson disease; **MRI**, magnetic resonance imaging; **RA/LA**, Right/Left Anterior Border of Red Nucleus; **RS/LS**, Right/Left Superior Border of Red Nucleus; **RL/LL**, Right/Left Lateral Border of Red Nucleus.

2.1 Introduction

Deep brain stimulation of the subthalamic nucleus (STN DBS) is an established surgical therapy for medically refractory Parkinson's disease (PD) [1]. In well-selected patients, STN DBS improves resting tremor, bradykinesia, rigidity and levodopa-induced dyskinesias, in a manner superior to best medical therapy [2,3]. With the success of the therapy worldwide, thousands of patients have been treated with STN DBS for PD in the past 25 years [4].

While the ideal stimulation site in the STN region is not known precisely, it is hypothesized that the active contact of the DBS electrode should be located in the dorsolateral (motor) region of the STN [5-8]. Accurate targeting of the STN during DBS surgery is essential, as small differences in DBS electrode localization can dramatically influence clinical outcome [9,10]. Stimulation outside of the motor STN is thought to produce side effects such as cognitive decline and behavioral changes reported in nearly half of STN DBS cases [11-13]. However, targeting the STN can be very challenging. The STN is small (158 mm^3) and poorly visualized on conventional (1.5T) MRI. Furthermore, it is often indistinguishable from the adjacent substantia nigra (SN) without the use of high field-strength (3T-9.4T) MRI, which is not widely available around the world [14].

To circumvent the limitations to direct STN visualization on conventional 1.5T MRI, neurosurgeons have utilized a combination of pre-surgical indirect targeting techniques and intraoperative microelectrode recordings to target the STN for DBS surgery [15]. These pre-surgical indirect techniques are based on the position of the STN relative to internal fiducial markers as imaged on MRI, such as the anterior and posterior commissures, according to neuroanatomical atlases [6-8,16,17].

Among these indirect techniques, the most commonly used are based upon the location of the mid-commissural point (MCP) [18-20] or the borders of the red nucleus (RN) [15,17] (Table 2-1), although other targeting approaches have been proposed [21,22]. Optimization of pre-surgical indirect targeting methods can reduce the number of surgical passes, thus reducing the risk of bleeding and the length of surgery [10]. Further, although microelectrode recording (MER) can assist STN targeting with the availability of a trained electrophysiologist, the MER has been reported to increase the risk of bleeding [10,23]. These factors motivate the continued use of indirect targeting techniques during STN DBS surgery.

	MCP-Based Targeting	**RN-Based Targeting**
X	12 mm lateral	3 mm lateral of lateral border
Y	3-4 mm posterior	Y-coordinate of anterior border
Z	3-5 mm inferior	2 mm inferior of superior border

Table 2-1. Indirect targeting of the STN for DBS surgery

Determining the relative quality of indirect STN targeting techniques is of broad interest to neurosurgeons, particularly at international centers or in intraoperative MR settings where the absence of high field strength MR imaging (> 1.5T) make direct STN targeting difficult. Two measures of targeting quality are of interest: accuracy and precision. Accuracy is the measure of the degree of closeness between the prediction of a quantity and its actual value. For example the prediction of the STN midpoint will be close to its actual location in an accurate targeting technique. Precision, by contrast, is the measure of the degree of variability in repeated applications of the targeting technique. For example, if the distance from the predicted STN location to its actual location is highly variable across patients, the targeting technique has low precision.

Previous studies have evaluated targeting techniques by comparing their predictions to the coordinates of the most efficacious, active DBS electrode contact [17]. While the ideal stimulation site in the STN region is not known precisely, it is hypothesized that the active contact of the DBS electrode should be located in the dorsolateral (motor) region of the STN [5-8]. The challenge of these studies is that the location of the DBS electrode, and therefore the location of the most efficacious contact, is itself constrained by and dependent upon the targeting method used during surgery. With the development of a validated 3T MRI protocol to visualize the STN [1], the opportunity arises to evaluate targeting methods without this limitation. Determining which targeting method most reliably predicts the location of the midpoint of the STN may allow neurosurgeons to target the dorsolateral region of the STN more reliably and efficiently.

In this study, we locate the midpoint of the MR-visualized STN (Figure 2-1). We then compare the accuracy and precision of MCP- and RN-based targeting methods relative to this location. Since we are able to visualize the midpoint of the STN directly, we then evaluate the impact of neuroanatomical variability, such as changes in third-ventricle size, on STN location. We utilize regression analysis to optimize the indirect targeting model and to compare this optimization with traditional MCP- and RN-based targeting of the STN. Finally, we evaluate RN-based targeting utilizing images at 1.5T field strength compared to RN-based targeting utilizing images at 3T field strength. Taken together, our findings suggest that neurosurgeons employing RN-based indirect targeting may expect more consistent results than others employing MCP-based indirect targeting.

2.2 Methods

2.2.1 Patient Selection

We evaluated the 3T MR images of 58 patients who had undergone bilateral STN DBS for advanced idiopathic PD (42 men, 16 women, age mean ± SD 63 ± 7 years, range 46-78 years). Selection criteria for DBS included a diagnosis of idiopathic PD, with the presence of motor fluctuations not optimally managed with medications, or severe levodopa-unresponsive tremor. Patients with contraindications to 3T MRI scanning, structural abnormalities on preoperative MRI, or dementia by neuropsychological testing were excluded from the study. We performed the study in accordance with the policies of the Medical Institutional Review Board of the University of Michigan.

2.2.2 MR Imaging and Analysis

Patients under evaluation for DBS surgery received pre-operative volumetric 3T MRI (Philips Achieva, Philips, Amsterdam, Netherlands) scans. The 3T MRI protocol was developed by our group, optimized for STN visualization, and has been validated against cadaveric anatomical studies and intraoperative electrophysiology [1]. The images were oriented in Talairach coordinate space along the intercommissural and midsagittal planes (Analyze 9.0, AnalyzeDirect Inc.,Overland Park, KS). Consistent with neurosurgical convention, the mid-commissural point (MCP) was designated as the origin. Positive X, Y, and Z directions were defined as left, anterior, and inferior, consistent with targeting using the Leksell Stereotactic Frame (Elekta AB, Stockholm, Sweden). Windowing of the 3T MR data for visualization was uniformly centered at the level that maximized contrast between STN and substantia nigra (SNR) and a width twice that amount, to minimize image measurement variability.

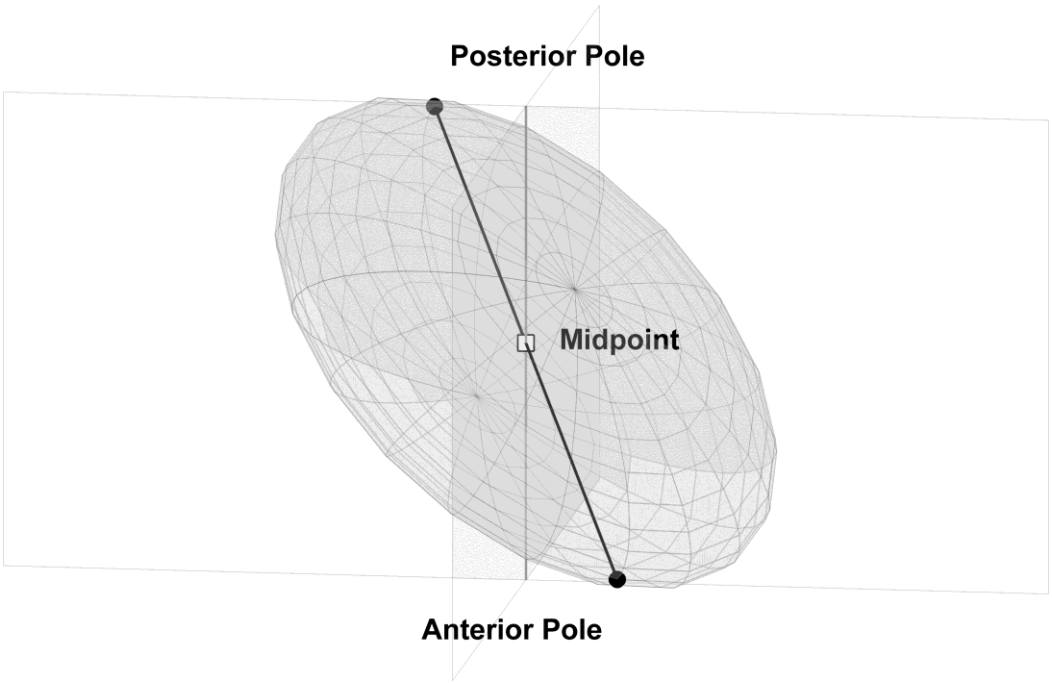

Figure 2-1. Coordinate determination of the STN midpoint. A graphical representation of the right STN is shown against coronal and sagittal planes. Anterior and posterior poles are defined in the coronal plane at the MR-visualized STN border. The STN midpoint is defined as equidistant between anterior and posterior poles.

Since the shape of the STN is not precisely ellipsoidal, we defined the midpoint of the STN as the location midway between the oral and caudal poles of the STN, which were selected on coronal MRI for closest correspondence to a well-established atlas of the human brain (Atlas of the Human Brain, plates 31-38) [24] (Figure 2-1). Our method is consistent with previously published methodology on determining the midpoint of the STN [9]. Coordinates of the RN borders were measured as defined in prior studies [15,17]. Briefly, the anterior, lateral, and superior borders were selected as the most anterior (axial plane), lateral (axial plane), and superior (coronal plane) points on volumetric 3T MRI in Talairach orientation.

In addition to STN midpoint location, whole-brain neuroanatomical parameters were measured as follows (35 men, 14 women, age mean ± SD 63 ± 7 years, range 46-78 years; 9 patients in the original group were excluded due to incomplete whole-brain imaging data): Brain length was measured as maximal antero-posterior dimension in the intercommissural plane on either side of the midline. Brain width was measured as the distance between insular cortical pia at the anterior commissure and temporoparietal cortical pia at the posterior commissure. Frontal horn width was measured as the maximal lateral ventricular width on axial slices. Third ventricular width was measured in the intercommissural plane at the mid-commissural point. Brain height was measured as the maximal vertical length in coronal images at the anterior commissure. All anatomical measurements were performed by the neurosurgeon performing the DBS surgeries (PGP) to minimize inter-observer variability.

To allow comparison between imaging field strengths, RN-based indirect targeting coordinates were calculated for 10 patients who had received 3T imaging with our validated protocol as well as 1.5T T2-weighted imaging (TR 5550, TE 82, 2 mm slice thickness). Images at 1.5T were oriented in Talairach coordinate space through co-registration (Analyze 9.0, AnalyzeDirect Inc.,Overland Park, KS). Coordinates of the RN borders were measured in identical and blinded fashion to images acquired at 3T.

2.2.3 Statistical Methods

Statistical analysis was performed using commercially available software: SAS (SAS Institute Inc., Cary, NC), Excel (Microsoft Inc., Redmond, WA) and MATLAB (Mathworks, Natick, MA). For all comparisons, statistical significance is defined at the $p < .05$ level. Except where otherwise noted, coordinate data are

reported as mean ± 95% confidence interval (CI). Comparisons of coordinates were performed with two-tailed paired t-tests for non-independent data. The Bonferroni correction was utilized for multiple comparisons. Comparisons of the precision of standard RN-based targeting and novel targeting methods were performed with right-tailed F-tests. We compared the variances in each coordinate on each side of the brain under the null hypothesis that the variance of two normal populations are the same and the alternative hypothesis that the variance of the standard RN-targeting population is greater than the variance of the model RN-targeting population. The best simple linear regression model for each coordinate was determined as the model with the highest R^2 value that had statistically significant parameter estimates ($p < 0.05$). For each linear regression model, the data were tested for homoscedasticity with the Kolmogorov-Smirnov test. Sources of statistical variability in our data include quantization effects due to voxel representation intrinsic to MR imaging and human error in measurement [1].

2.3 Results

2.3.1 STN Midpoint Coordinates

Table 2-2 reports the X-, Y-, and Z-coordinate locations of the right and left STN in our study (mean ± 95% CI, n = 58). The STN midpoints are symmetrical within 95% CI limits for individual patients. The MCP is designated as the origin and left, anterior, and superior represent increasing X, Y, and Z coordinates, respectively. With this convention, the right STN midpoint was located at X = -10.90 ± 0.31 mm, Y = -0.66 ± 0.35 mm, Z = -3.63 ± 0.29 mm. The left STN midpoint was located at X = 11.41 ± 0.28, Y = -1.23 ± 0.34, Z = -3.88 ± 0.31. These values compare well with traditional targeting coordinates for the dorsolateral STN (Table 2-1).

	X (mm)	Y (mm)	Z (mm)
R STN	-10.90 ± 0.31	-0.66 ± 0.35	-3.63 ± 0.29
L STN	11.41 ± 0.28	-1.23 ± 0.34	-3.88 ± 0.31

Table 2-2. Coordinates of the STN midpoint determined by validated 3T MRI. Measurements are reported as mean ± 95% CI (N = 58).

Coordinate	R Brain Length	L Brain Length	Brain Width at AC	Brain Width at PC	Frontal Horn Width	Third Ventricle Width at MCP	Brain Height
R STN X					-0.33 *p = 0.02*	-0.54 *p < 0.01*	
R STN Y							
R STN Z	-0.42 *p < 0.01*	-0.40 *p = 0.04*					
L STN X					0.37 *p < 0.01*	0.51 *p < 0.01*	
L STN Y							
L STN Z	-0.35 *p = 0.01*	-0.34 *p = 0.02*					

Table 2-3. Pearson's correlation coefficients for STN coordinates and neuroanatomical parameters. Empty cells indicate the absence of statistically significant correlation (N=49).

2.3.2 Correlation of STN Midpoint Coordinates and Neuroanatomical Parameters

Table 2-3 reports the correlation between right and left STN midpoint coordinates and major neuroanatomical parameters, as defined in our *Methods*. Significant correlation for the laterality (X-coordinate) of the STN is present for CSF spaces in the brain. Correlation between laterality and maximal frontal horn width is weaker, though statistically significant (Right: r = -0.33, p = 0.02; Left: r = 0.37, p < 0.01). By comparison, we find stronger correlation between STN laterality and third ventricle width (Right: r = -0.54, p < 0.01; Left: r = 0.51, p < 0.01). Linear regression of bilateral STN midpoint separation and third ventricular width yields strong correlation (Figure 2-2), with third-ventricular width accounting for 40% of the variance in STN separation (R^2 = 0.4). Juxtaposed with this strong overall explanatory value, the individual lateral coordinates of the right and left STNs are only weakly explained by the width of the third ventricle (Right: R^2 = 0.29; Left: R^2 = 0.26). In the rostrocaudal dimension, there are no statistically significant correlations observed between the Y-coordinate of the STN midpoint and any of the neuroanatomical parameters that we examined. In the dorsoventral dimension,

there are significant correlations bilaterally between brain length (maximal antero-posterior dimension in the intercommissural plane) and the Z-coordinate of the STN midpoint (Right: r = -0.40 to -0.42, p = 0.01; Left: r = -0.34 to -0.35, p = 0.01). Empty cells in the table indicate the absence of statistically significant correlations.

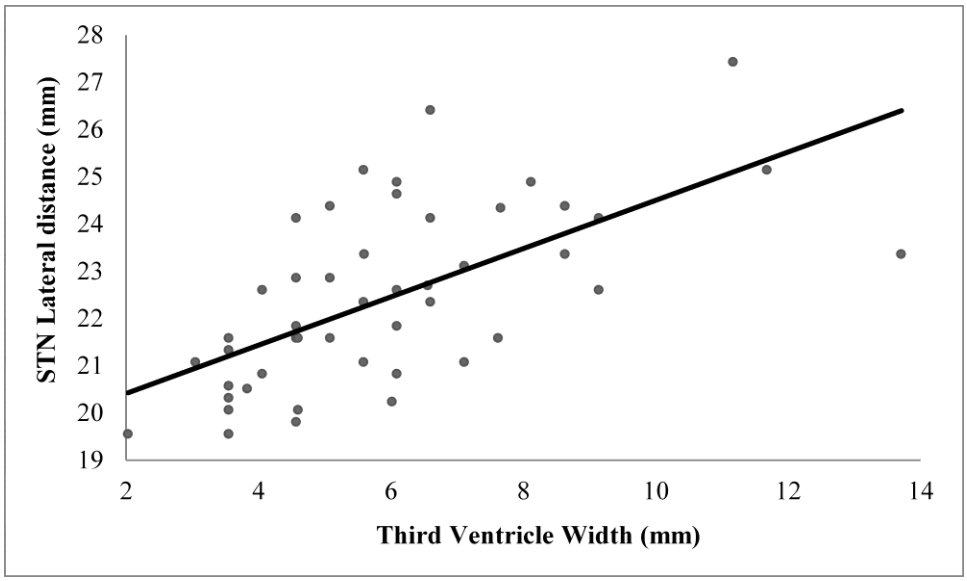

Figure 2-2. Linear regression of STN midpoint separation and third ventricular width. With greater third ventricular width, the lateral distance between bilateral STN midpoints increases.

2.3.3 Comparison of MCP- and RN-based Targeting Accuracy and Precision

Figure 2-3 compares the results of MCP- and RN-based targeting accuracy and precision for the coordinates of the STN midpoint. Absolute errors in targeting are plotted for each of the coordinates and targeting methods, using optimized offsets for our dataset. Average absolute errors in targeting are lower for RN-based targeting (mean ± SD, Right and Left pooled; X, Y, Z: 0.67 ± 0.45 mm, 0.77 ± 0.54 mm, 0.56 ± 0.40 mm) than for MCP-based targeting (mean ± SD, Right and Left pooled; X, Y, Z: 0.91 ± 0.70 mm, 1.04 ± 0.81 mm, 0.92 ± 0.71 mm) for each coordinate (p < .01 in all cases), indicating that indirect RN-based targeting is

more accurate than MCP-based targeting. Standard deviations in the absolute errors, as indicated by the error bars in the figure, are a measure of targeting precision. For all coordinates, RN-based targeting is also significantly more precise than MCP-based targeting (F-test, $p < 0.05$ for each coordinate direction).

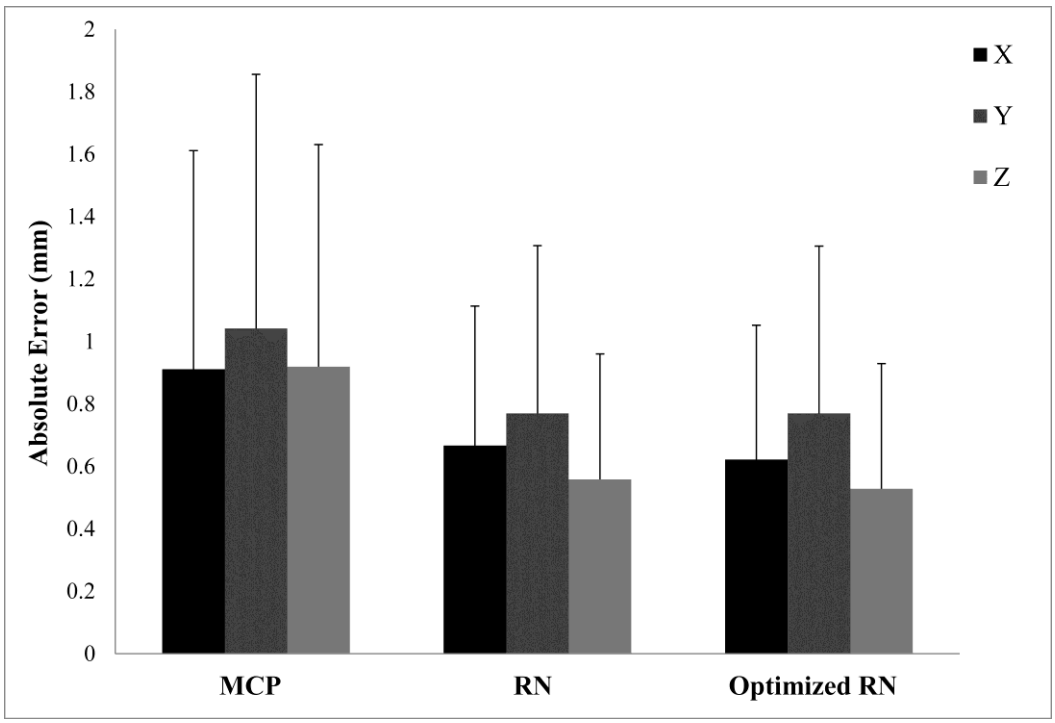

Figure 2-3. Comparison of MCP- and RN-based targeting accuracy. Absolute errors in targeting (mean ± SD) are plotted for MCP, RN, and Optimized RN models. Greyscale indicates X, Y, and Z coordinates.

2.3.4 Creating an Optimized Targeting Model

To create an optimized targeting model, we evaluated the targeting parameters (location relative to MCP, RN borders, neuroanatomical parameters) with regression analysis. Table 2-4 reports the final optimized model parameters. Regression analysis eliminated the MCP coordinates and all other measured neuroanatomical parameters as statistically insignificant. By contrast, the borders

of the RN correlate strongly with STN midpoint coordinates, with slopes for all regression models approximately equal to one (range 0.91 to 1.05). The best-optimized predictors for the Y-coordinate of the right STN and all of the left STN coordinates are the same used during standard RN-based targeting (lateral, anterior, and superior RN borders for X, Y, and Z STN midpoint coordinates, respectively). For the right STN midpoint, however, the X-coordinate is better predicted by the superior border of the RN than the lateral border (R^2 = .56 vs. R^2 = .48), while the Z-coordinate is better predicted by the anterior border of the RN than the superior border (R^2 = .70 vs. R^2 = .65). These small improvements in predictive power result in a small but statistically significant improvement in accuracy for the optimized regression model, without improvement in precision (Fig. 2-3).

Regression Line	R^2
RSTNx = 1.05 × RSx – 5.77	.56
RSTNy = 0.94 × RAy + 1.42	.45
RSTNz = 0.96 × RAz + 1.39	.70
LSTNx = 0.91 × LLx + 3.27	.58
LSTNy = 0.98 × LAy + 1.05	.55
LSTNz = 1.04 × LSz – 1.75	.65

Table 2-4. Results of STN-RN regression modeling. (N = 58)

2.3.5 Comparison of Targeting Parameters

Table 2-5 presents the final optimized STN midpoint targeting parameters for MCP-based, RN-based, and regression optimized targeting methods. MCP-based midpoint targeting parameters are equivalent to values found in STN midpoint measurements. Optimized targeting parameters are determined through linear regression. Both RN-based and optimized targeting strategies are significantly more accurate for individual patients ($p < 0.05$) and precise ($p < 0.002$) than MCP-based targeting. RN-based and regression optimized RN-based methods are not

statistically distinguishable. RN-based coordinates for the STN midpoint compare well with traditional targeting coordinates for the dorsolateral STN (Table 2-1).

	RSTNx	**RSTNy**	**RSTNz**
MCP	MCPx – 10.90	MCPy – 0.66	MCPz – 3.63
RN	RLx – 2.75	RAy + 1.55	RSz – 1.68
Optimized RN	1.05×RSx – 5.77	0.94×RAy + 1.42	0.96×RAz + 1.39
	LSTNx	**LSTNy**	**LSTNz**
MCP	MCPx + 11.41	MCPy – 1.23	MCPz – 3.88
RN	LLx + 2.55	LAy + 1.08	LSz – 1.84
Optimized RN	0.91×LLx + 3.27	0.98×LAy + 1.05	1.04×LSz – 1.75

Table 2-5. STN midpoint targeting parameters. MCP: midcommissural point; RN: red nucleus; STN: subthalamic nucleus; RL/LL: right and left lateral; RA/LA: right and left anterior; RS/LS: right and left superior; x,y,z subscripts indicate corresponding coordinate directions (N = 58).

2.3.6 Evaluation of RN-Based Targeting Results at 1.5T

Figure 2-4 illustrates 3T (Fig. 2-4A) and 1.5T (Fig 2-4B) co-registered coronal MRI images for the same patient. The RN is visible in both 1.5T and 3T images (white arrows), while the STN and SNR are only visible in 3T images. As expected with imaging at lower field strength, tissue contrast and delineation of structural borders are less distinct at 1.5T than 3T.

To evaluate the application of our 3T RN-based targeting methodology to 1.5T, we performed a blinded comparison of RN boundary coordinates in 10 patients who had imaging performed at both field strengths. Maximal RN-based targeting coordinate differences between 3T and 1.5T images were less than one voxel, ranging from -0.41 ± 0.17 mm (mean ± SEM) for the right superior Z-coordinate (RSz) to 0.27 ± 0.22 mm for the left anterior Y-coordinate (RAy). None of the indirect targeting differences between images at 3T and 1.5T were statistically significant.

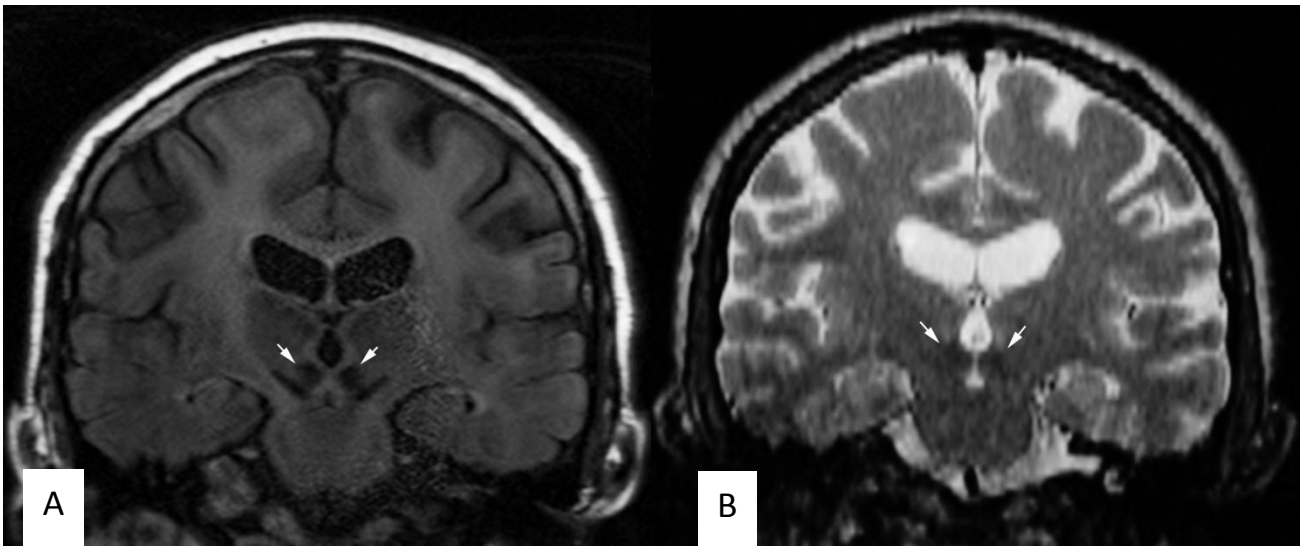

Figure 2-4. Comparison of coronal 3T and 1.5T MRI images for RN visualization in the same patient. The RN is well visualized at both 3T (A) and 1.5T (B). By contrast the STN and SNR are only well visualized at 3T.

2.4 Discussion

Deep Brain Stimulation of the STN region is the predominant surgical therapy for Parkinson's disease. Accurate surgical targeting is essential for optimal patient outcomes. With advances in magnetic-field strength, direct visualization of the STN on MR imaging has become possible in some centers. However, in the majority of neurosurgical centers throughout the world, where advanced 3T MRI imaging techniques are not available, indirect and atlas-based STN targeting techniques are most often utilized. A detailed evaluation of the accuracy of the two predominant indirect targeting techniques, MCP-based and RN-based targeting, is therefore of significant interest to neurosurgeons, with the potential to reduce surgical complexity and to shorten operative times.

We have previously reported a validated 3T MRI protocol to directly visualize the STN [1]. Our protocol is unique in that our MR-visualized STN has been validated against both published human anatomical studies and intraoperative electrophysiology. In this study, we utilize this validated 3T MRI protocol to evaluate the location of the STN midpoint, to compare MCP- and RN-based STN-targeting techniques, and to evaluate the influence of multiple neuroanatomical parameters on STN location. Our study suggests that RN-based indirect targeting of the STN is both more accurate and more precise than MCP-based indirect targeting. We further determine that coordinates predicted by RN-based targeting at 3T match those predicted at 1.5T, indicating that neurosurgeons may wish to consider favoring RN-based over MCP-based indirect targeting when performing STN DBS surgery.

2.4.1 Correlation of STN Midpoint Coordinates and Neuroanatomical Parameters

We find significant correlation between STN location and neuroanatomical parameters, including CSF spaces in the brain. Strongest correlation occurs between third-ventricle width and STN laterality. However, explicitly incorporating third ventricle width into surgical planning is not required to target the STN: ipsilateral RN coordinates account well for STN displacements due to changes in the size of CSF spaces, as indicated by regression analysis. Similarly, RN-related variables account better for the dorsoventral location of the STN midpoint than brain-length neuroanatomical variables. These findings suggest that RN-based indirect targeting automatically compensates for multiple sources of anatomic variation in STN targeting. Incorporation of additional neuroanatomical variables into indirect RN-based STN targeting does not appear to improve targeting accuracy to a significant degree. By comparison, MCP-based targeting, with fixed lateral displacement traditionally, does not incorporate neuroanatomical

parameters such as third-ventricle width or shifts in STN location relative to the MCP.

2.4.2 Comparison of MCP- and RN-based Targeting Accuracy and Precision

Our analysis confirms and quantifies the superiority of RN-based indirect STN targeting over MCP-based targeting, in terms of accuracy and precision (Figure 2-3). Absolute error, a measure of targeting accuracy, is lower for RN-based targeting than for MCP-based targeting in each coordinate dimension. Improvements in average accuracy for RN-based targeting over MCP-based targeting are 0.2 mm, 0.2 mm, and 0.3 mm in the X-, Y-, and Z-coordinates, respectively. In addition, RN-based targeting has superior precision, with reduced variability across patients. Based upon these findings, neurosurgeons may routinely consider RN-based indirect targeting over MCP-based targeting.

A recent review of MR-based targeting techniques by Brunenberg et al. reported conflicting results regarding the superiority of RN-based targeting over MCP-based targeting [14]. Andrade-Souza et al. reported that the RN is the more reliable internal fiducial marker for determining the "optimal" contact in STN DBS [17]. The challenge of such analysis is that the location of the DBS electrode, and therefore the location of the most efficacious contact, is itself constrained by and dependent upon the targeting method chosen by the neurosurgeon. Our study compares indirect RN-based and MCP-based targets against the midpoint of the MR-visualized STN, the location of which is independent of targeting techniques. However, the relationship of the STN midpoint to the locus of clinically optimal stimulation remains to be defined precisely. Our findings indicate that the STN midpoint is anterior and medial to traditional indirect targeting coordinates. This is consistent with clinical targeting to the dorsolateral (motor) portion of the STN. To

provide further clinical application of our anatomical finding, a follow-up study is underway to determine the optimal locus of DBS stimulation relative to the MR-visualized STN midpoint.

2.4.3 Creating an Optimized Targeting Model

We explored the possibility of optimizing RN-based targeting through the use of neuroanatomical and RN-based variables with highest correlation to STN coordinates and regression analysis. We find that the optimized RN-based targeting methods are statistically indistinguishable from traditional RN-based targeting, despite higher correlation values. Greater statistical resolution may be achieved with higher sample size. However, the improvement in accuracy (< 0.1 mm) appears likely to be clinically insignificant. Our results therefore support the adoption of standard RN-based indirect targeting over more complex RN-based targeting techniques.

2.4.4. Evaluation of RN-Based Targeting Results at 1.5T

In this study, we utilize a validated 3T MR imaging protocol to evaluate MCP- and RN-based indirect targeting of the STN. Our aim is to determine and to compare the accuracy and precision of these commonly utilized methods of STN targeting for neurosurgeons lacking high-field MRI capabilities at their centers. We find that RN-based targeting is both more accurate and more precise than MCP-based targeting at 3T. An important additional step is the validation of these results at 1.5T. RN visualization is protocol-dependent. We find that the RN (but not the STN) can be well visualized at 1.5T (Fig. 2-4) and that differences in targeting parameters calculated from 3T and 1.5T images are clinically and statistically insignificant. RN-based targeting at 1.5T produces the same target coordinates for use during STN DBS surgery as targeting at 3T.

2.4.5 Comparison with Previous Work on STN Localization

Our results compare well with STN midpoint coordinates (11.8 mm lateral, 1.3 mm posterior, 4.0 mm inferior) in the Schaltenbrand-Wahren (S-W) atlas as well as previous study at 1.5T magnetic field strength, which pooled right and left STN coordinates to reduce statistical variability [9]. Several previous studies have reported the inferiority of direct targeting alone with 1.5T MRI compared to a combination of indirect targeting methods [17,25,26]. However, higher field strength appears to allow for greater localization accuracy. Several recent studies have reported that 3T MR imaging is a more accurate method for direct targeting of the STN for DBS surgery [27,28]. Our study extends these findings at 1.5T and 3T to measure the location of the STN midpoint directly at 3T MR field strength. Significantly, when pooled, our measurements for the center of right and left STNs agree well with the earlier measurements of Daniluk et al.

2.4.6 Previous Evaluation of MCP- and RN-based Targeting

We are not the first to suggest the superiority of RN-based targeting to MCP-based targeting for STN targeting [15,17]. However, a statistical evaluation of targeting techniques at high field strength with a validated MR imaging protocol has been unavailable up to the present time. Traditional MCP-based indirect targeting of the STN remains dominant in the neurosurgical community. In a review of publications on MR-based targeting techniques for STN DBS, MCP-based targeting was utilized far more frequently than RN-based targeting [14]. In addition, studies performed at 1.5T field strength have questioned the use of the RN as a reliable internal fiducial marker for STN location [29]. Danish et al. reported that 1.5T MRI is inadequate to delineate the relationship between the STN and RN borders. However, at the voxel sizes in each dimension utilized in that

study (> 2 mm), the image resolution at the time of that study may have been inadequate compared to currently available technology [29]. Confounding results may also be MR protocol specific, as the RN may be difficult to visualize at 1.5T without optimization of scanning parameters. In our 1.5T MR imaging protocol, the RN is well visualized, while both RN and STN are clearly visualized in our validated 3T imaging protocol. Our comparison between 1.5T-based and 3T-based RN border measurements demonstrates that 1.5T MRI is equivalent to 3T MR in terms of measuring RN borders, and therefore is appropriate for indirect STN targeting. Another historical criticism of RN-based targeting has been that the parameters for targeting were derived from the SW Atlas [17]. The atlas represents one representative brain specimen and thus does not capture variability among PD patients [9]. In the present study, validated MR imaging in a large population of PD patients allowed quantitative evaluation of targeting uncertainty.

2.5 Conclusions

RN-based indirect STN targeting is significantly more precise than MCP-based STN targeting, and accommodates broad changes in anatomic parameters, such as third ventricular width. Our analysis suggests that neurosurgeons employing RN-based indirect targeting may expect more consistent results than others employing MCP-based indirect targeting at 1.5T. Future work is required to determine the optimal site of DBS stimulation relative to the STN midpoint and to incorporate this information into RN-based indirect targeting parameters during DBS surgery.

Acknowledgments: We thank Matthew Leach and Erin C. Conrad for technical assistance.

Disclosures: The authors report no conflict of interest concerning the materials or methods used in this study or the findings specified in this chapter. The entirety of this chapter is in press: Houshmand, L. et al. "Evaluating Indirect Subthalamic Nucleus Targeting with Validated 3-Tesla Magnetic Resonance Imaging". *Stereotactic and Functional Neurosurgery*, 92(6), 2014.

2.6 References

1. Patil, P.G., et al., The anatomical and electrophysiological subthalamic nucleus visualized by 3-T magnetic resonance imaging. Neurosurgery, 2012. **71**(6): p. 1089-95; discussion 1095.

2. Deuschl, G., et al., A randomized trial of deep-brain stimulation for Parkinson's disease. The New England journal of medicine, 2006. **355**(9): p. 896-908.

3. Schuepbach, W.M., et al., Neurostimulation for Parkinson's disease with early motor complications. The New England journal of medicine, 2013. **368**(7): p. 610-22.

4. Benabid, A.L., et al., Deep brain stimulation of the subthalamic nucleus for the treatment of Parkinson's disease. The Lancet Neurology, 2009. **8**(1): p. 67-81.

5. Hamel, W., et al., Deep brain stimulation of the subthalamic nucleus in Parkinson's disease: evaluation of active electrode contacts. Journal of Neurology, Neurosurgery & Psychiatry, 2003. **74**(8): p. 1036-1046.

6. Lanotte, M.M., et al., Deep brain stimulation of the subthalamic nucleus: anatomical, neurophysiological, and outcome correlations with the effects of stimulation. Journal of Neurology, Neurosurgery & Psychiatry, 2002. **72**(1): p. 53-58.

7. Saint-Cyr, J.A., et al., Localization of clinically effective stimulating electrodes in the human subthalamic nucleus on magnetic resonance imaging. Journal of neurosurgery, 2002. **97**(5): p. 1152-1166.

8. Yelnik, J., et al., Localization of stimulating electrodes in patients with Parkinson disease by using a three-dimensional atlas-magnetic resonance imaging coregistration method. Journal of Neurosurgery, 2003. **99**(1): p. 89-99.

9. Daniluk, S., et al., Assessment of the variability in the anatomical position and size of the subthalamic nucleus among patients with advanced Parkinson's disease using magnetic resonance imaging. Acta Neurochirurgica, 2009. **152**(2): p. 201-210.

10. Benabid, A.L., Deep brain stimulation for Parkinson’s disease. Current Opinion in Neurobiology, 2003. **13**(6): p. 696-706.

11. Temel, Y., et al., The functional role of the subthalamic nucleus in cognitive and limbic circuits. Progress in Neurobiology, 2005. **76**(6): p. 393-413.

12. Temel, Y., et al., Behavioural changes after bilateral subthalamic stimulation in advanced Parkinson disease: A systematic review. Parkinsonism & related disorders, 2006. **12**(5): p. 265-272.

13. Voon, V., et al., Deep brain stimulation: Neuropsychological and neuropsychiatric issues. Movement disorders, 2006. **21**(S14): p. S305-S327.

14. Brunenberg, E.J., et al., Magnetic resonance imaging techniques for visualization of the subthalamic nucleus. Journal of neurosurgery, 2011. **115**(5): p. 971-84.

15. Bejjani, B.P., et al., Bilateral subthalamic stimulation for Parkinson's disease by using three-dimensional stereotactic magnetic resonance imaging and electrophysiological guidance. Journal of neurosurgery, 2000. **92**(4): p. 615-625.

16. Hamani, C., et al., Correspondence of microelectrode mapping with magnetic resonance imaging for subthalamic nucleus procedures. Surgical neurology, 2005. **63**(3): p. 249-253.

17. Andrade-Souza, Y.M., et al., Comparison of three methods of targeting the subthalamic nucleus for chronic stimulation in Parkinson's disease. Neurosurgery, 2005. **56**(4): p. 360-368.

18. Benabid, A.L., et al., Deep brain stimulation of the subthalamic nucleus for Parkinson's disease: methodologic aspects and clinical criteria. Neurology, 2000. **55**(12): p. S40-S44.

19. Starr, P.A., et al., Implantation of deep brain stimulators into the subthalamic nucleus: technical approach and magnetic resonance imaging-verified lead locations. Journal of neurosurgery, 2002. **97**(2): p. 370-87.

20. Ashkan, K., et al., Variability of the subthalamic nucleus: the case for direct MRI guided targeting. British Journal of Neurosurgery, 2007. **21**(2): p. 197-200.

21. Caire, F., et al., The mamillothalamic tract is a good landmark for the anterior border of the subthalamic nucleus on axial MR images. Stereotactic and functional neurosurgery, 2011. **89**(5): p. 286-90.

22. Deogaonkar, M., et al., Subthalamic nucleus targeting using interpeduncular cistern as an internal landmark. Neurosurgery, 2011. **69**(2 Suppl Operative): p. ons225-9.

23. Hariz, M.I. and H. Fodstad, Do Microelectrode Techniques Increase Accuracy or Decrease Risks in Pallidotomy and Deep Brain Stimulation? Stereotactic and functional neurosurgery, 1999. **72**(2-4): p. 157-169.

24. Mai, J.K., J. Assheuer, and G. Paxinos, Atlas of the human brain. 2nd ed. 2004, Amsterdam ; Boston: Elsevier Academic Press. viii, 246 p.

25. Zonenshayn, M., et al., Comparison of anatomic and neurophysiological methods for subthalamic nucleus targeting. Neurosurgery, 2000. **47**(2): p. 282-294.

26. Cuny, E., et al., Lack of agreement between direct magnetic resonance imaging and statistical determination of a subthalamic target: the role of electrophysiological guidance. Journal of neurosurgery, 2002. **97**(3): p. 591-597.

27. Cheng, C.H., et al., 1.5T versus 3T MRI for targeting subthalamic nucleus for deep brain stimulation. British Journal of Neurosurgery, 2013: p. 1-4.

28. Slavin, K., et al., Direct visualization of the human subthalamic nucleus with 3T MR imaging. American journal of neuroradiology, 2006. **27**(1): p. 80-84.

29. Danish, S.F., et al., Conventional MRI is inadequate to delineate the relationship between the red nucleus and subthalamic nucleus in Parkinson's disease. Stereotactic and functional neurosurgery, 2006. **84**(1): p. 12-18.

Chapter 3

Individualized Thalamic Segmentation and Tissue Activation Modeling in Deep Brain Stimulation for Essential Tremor

Abstract

Background/Aims: Thalamic deep brain stimulation (DBS) is the dominant neurosurgical therapy for the treatment of medically refractory essential tremor (ET). The mechanisms of DBS-mediated tremor control remain unknown. However, computational modeling of DBS-induced electrical fields and volumes of tissue activated (VTA) have improved our understanding of the influence of lead location and stimulation parameters on clinical efficacy. To date, patient-specific computational studies have relied upon atlas-based representations of patient anatomy for both thalamic segmentation and VTA modeling. However, recent advances in diffusion-tensor magnetic resonance imaging (DTI) have raised the possibility of an atlas-independent, patient-specific approach. In this study, we present a fully patient-specific methodology for DTI-based thalamic segmentation and VTA modeling in patients with ET and compare this approach to more traditional atlas-based modeling.

Methods: Our study includes 10 patients treated with unilateral, left thalamic DBS for ET at our institution. For each subject, we compared the results of atlas-based and patient-specific thalamic segmentation and VTA modeling at clinically efficacious stimulation settings. Patient-specific thalamic segmentation was performed utilizing a novel, modified k-means clustering algorithm to delineate individual thalamic nuclei. Patient-specific VTA modeling was performed by calculating the region of neuronal activation from individual DTI-derived conductivity tensor fields.

Results: Thalamic segmentations based on individual DTI data compared well with atlas-based results. All 10 of 10 patient-specific VTAs for the active contact at the clinically determined stimulation settings were localized to the motor thalamus. By comparison, only 9 of 10 atlas-based VTAs overlapped with the motor thalamus for the same stimulation settings. The distance of the active contact to the motor thalamus centroid was 4.6 ± 1.7 mm for patient-specific segmentations and 5.0 ± 2.9 for the atlas-based approach, although this improvement was not statistically significant.

Conclusions: While traditional atlas-based thalamic segmentation and VTA modeling provides reliable means of DBS targeting and mechanistic study, improved precision may be possible with a patient-specific approach based on individual DTI imaging data.

Abbreviations: **DBS**, deep brain stimulation; **ET**, Essential Tremor; **VTA**, Volume of Tissue Activated; **Vim**, Ventral Intermediate; **Vc**, Ventrocaudal; **MRI**, Magnetic Resonance Imaging; **DTI**, Diffusion Tensor Imaging; **AC**, Anterior Commissure; **PC**, Posterior Commissure; **A**, Anterior; **VA**, Ventral Anterior; **VLa**,

Ventral Lateral Anterior; **VLPd**, Ventral Lateral Posterior-dorsal ; **VLPv**, Ventral Lateral Posterior-ventral; **VPL**, Ventral Posterior Lateral; **VPM**, Ventral Posterior Medial; **VM**, Ventral Medial; **P**, Pulvinar; **MD**, Mediodorsal; **LD**, Lateral Dorsal; **LP**, Lateral Posterior; **CM**, Central Median; **CL**, Central Lateral; **LGN**, Lateral Geniculate Nucleus; **MGN**, Medial Geniculate Nucleus.

3.1 Introduction

Chronic, high-frequency deep brain stimulation (DBS) of the ventral lateral posterior-ventral (VLPv)—also known as the ventral intermediate (Vim) [1-4]—nucleus of the thalamus is the dominant surgical therapy for controlling medically-refractory kinetic and postural tremor in Essential Tremor (ET) [5-9]. The mechanisms underlying thalamic DBS are poorly understood for two reasons. First, despite its success in treating a variety of neurological conditions, the mechanism of DBS itself remains controversial [10-12]. Second, studying thalamic DBS has been difficult for researchers due to the challenge of establishing structure-function relationships in the thalamus, which has functionally distinct but poorly visualized nuclei [9].

While direct visualization of thalamic nuclei is not possible using conventional MRI [9], it has been proposed that diffusion tensor imaging (DTI) can help delineate nuclear boundaries [13-18]. Several computational thalamic segmentation methods exist based on this principle [15, 17-26], and the use of DTI in movement disorder surgery is an emerging trend [27]. Typically, neurosurgeons preoperatively target the thalamus with stereotactic atlas-derived coordinates and refine the target during surgery with intraoperative macrostimulation and microelectrode recordings [9]. Improved preoperative planning could reduce the need for microelectrode recordings, thus minimizing the risk of intracranial hemorrhage [28], and improve patient outcomes overall.

Computational modeling of the volume of tissue activated (VTA) in DBS has been used to study the stimulation locations and parameters for Parkinson's disease (PD) DBS [29-36], though these methods typically rely on brain atlas warping as a

means of comparison across subjects. To date, no group has analyzed the VTAs in ET DBS, and only three computational studies have investigated or modeled ET DBS [37-39] in any capacity. Therefore, we set out to combine the concepts of patient-specific thalamic nuclei segmentation and DBS VTA modeling.

In this study, we present the first individualized VTA model for thalamic DBS in 10 ET patients. We segmented patient thalami with a modified k-means clustering algorithm, and incorporated the results in a previously-published atlas-based VTA modeling system. We provide some preliminary comparisons of individualized and atlas-based modeling, leaving a detailed comparison for an accompanying study. This article describes our methodology, preliminary results, and discusses limitations and future work.

3.2 Materials and Methods

The overall objective of this study was to develop an individualized VTA model for thalamic DBS. This project integrated electrical and anatomical representations of the brain into a finite-element electric field modeling system for DBS [32]. Brain conductivity values were derived from diffusion tensor imaging (DTI). Thalamic anatomy was manually parcellated from pre-operative patient MRI scans, and then segmented into functionally distinct nuclei using a modified k-means clustering algorithm [15]. Stimulation volumes were then calculated for the most clinically-efficacious stimulation settings, and their overlaps with relevant anatomy were compared.

3.2.1 Patient Selection and Clinical Data

We retrospectively evaluated the VTAs of 10 ET patients who had undergone unilateral left Vim (VLPv) DBS for advanced idiopathic ET (6 men, 4 women, age mean ± SD 66 ± 7 years, range 49-74 years). Selection criteria for DBS included a diagnosis of idiopathic ET, with the presence of tremor no longer well-managed with medications. Patients with co-morbid neurological or psychiatric conditions were excluded. We performed the study in accordance with the policies of the Medical Institutional Review Board of the University of Michigan.

3.2.2 Image Data Acquisition and Analysis

3.2.2.1 MRI Scanning

Patients received pre-operative volumetric 3T MRI and DTI (Philips Ingenia, Philips, Amsterdam, Netherlands) scans for surgical trajectory planning and post-operative analysis. MR images were acquired using the protocol reported in [40] and were oriented in Talairach coordinate space along the intercommissural and midsagittal planes (Analyze 11.0, AnalyzeDirect Inc., Overland Park, KS). Consistent with neurosurgical conventions, the mid-commissural point (MCP) was designated as the origin. Positive X, Y, and Z directions are defined as right, anterior, and inferior, consistent with finite-element modeling software conventions (SCIRun 4.7, Scientific Computing Institute, Salt Lake City, UT).

DTI data were acquired on a 3T scanner (Philips Ingenia, Philips, Amsterdam, Netherlands) using a single-shot echo planar imaging sequence with a dS-SENSE parallel-imaging scheme (reduction factor = 2, field of view = 224 mm x 224 mm, 1 mm x 1 mm x 2 mm voxels). Diffusion weighting was encoded along 15

independent orientations with a b-value of 800 s/mm². One additional image without diffusion weighting (b = 0 s/mm²) was also acquired. DTI images were adjusted for "jitter" and then resampled using cubic spline interpolation to match the resolution of MR image. The DTI volumes were coregistered to 3T MR images, and the rigid transformation matrix from the co-registration was saved. Analyze's DTI module was used to calculate the eigenvalues and eigenvectors of the DTI volumes.

3.2.2.2. CT Scanning

Patients received post-operative CT scans 6-8 weeks after DBS surgery to confirm correct electrode placement using the CT protocol reported in [40]. CT images were oriented in Talairach space via coregistration to 3T MRI images, and the coordinates of the Medtronic 3387 DBS electrode contact points were recorded (Analyze 11.0, AnalyzeDirect Inc., Overland Park, KS).

For all image coregistrations, the Normalized Mutual Information algorithm [41] in Analyze's 3D Voxel Registration function was used, followed by manual adjustment to properly align the anterior and posterior commissures.

3.2.2.3 Conductivity Tensor Calculation

Diffusivity tensors were first calculated from DTI eigenvalues and eigenvectors in MATLAB (Mathworks, Natick, MA) using matrix diagonalization [42, 43]:

$$D = Q\Lambda Q^{-1} = Q\Lambda Q^{T}$$

where Q is the orthogonal eigenvector matrix of diffusion tensor D and Λ is the diagonal eigenvalue matrix of diffusion tensor D. Due to DTI coregistration to Talairach orientation, the diffusion tensors required re-orientation as follows [44]:

$$D' = RDR^T$$

where D' is the re-oriented diffusion tensor, D is the original diffusion tensor, and R is a rotation matrix representing the rotation that occurred during coregistration. R was found by calculating the polar decomposition of the upper 3x3 part of the 4x4 rigid transformation matrix from coregistration. Talairach-oriented diffusivity tensors were then converted to conductivity tensors as described by [45, 46].

3.2.3 Thalamic Segmentation

3D reconstructions of the thalamus and its functionally distinct nuclei were obtained for each patient in two steps: manual parcellation from MR images followed by semi-automatic segmentation with a modified k-means clustering algorithm [15]. Each thalamus was segmented into13 nuclei following the naming convention presented by the Morel histological atlas [47]: Anterior (A), Ventral Anterior (VA), Ventral Lateral Anterior (VLa), Ventral Lateral Posterior-dorsal (VLPd), Ventral Lateral Posterior-ventral (VLPv), Ventral Posterior Lateral (VPL), Ventral Posterior Medial (VPM), Ventral Medial (VM), Pulvinar (P), Mediodorsal (MD), Lateral Dorsal (LD), Lateral Posterior (LP), Central Median (CM). The Central Lateral (CL), Lateral Geniculate Nucleus (LGN), and Medial Geniculate Nucleus (MGN) were small enough to be excluded; in most cases, the LGN and MGN were assumed to not be visible based on the parcellation. Of particular interest was the VLPv nucleus, the target nucleus for ET DBS. The Morel atlas was selected over the Schaltenbrand-Wahren atlas for its simplicity

and because it was used in two prior k-means thalamic segmentation investigations [15, 48].

The k-means algorithm is a statistical clustering technique used in many fields. It allows a larger set of data to be broken up into a specified number of clusters based on a user-provided distance metric. It relies on four parameters [49]: (1) the number of clusters to be segmented, (2) a distance metric or combination of metrics, (3) initial coordinates of the cluster centroids, (4) a well-defined stopping point for the algorithm. The algorithm moves data into clusters in a way that minimizes the distance metric, iterating until the convergence criterion is reached. Following segmentation, we validated the algorithm by comparing pooled results against known anatomy from a histological atlas of the thalamus.

3.2.3.1 Thalamic Parcellation

The left thalamus was parcellated manually from high-resolution coronal MR images (Analyze 11.0, AnalyzeDirect Inc., Overland Park, KS). The thalamus was defined in the mediolateral axis by the third ventricle and the posterior limb of the internal capsule and in the dorsoventral axis by the lateral ventricles and the subthalamic nucleus [15]. All co-registrations, anatomical measurements, and parcellations were performed by one investigator (LH) to minimize inter-observer variability.

3.2.3.2 K-Means Clustering Algorithm

The initial centroids were selected by one investigator (LH) based on *a priori* information from the Morel histological atlas [47]. We selected a distance metric to take into account the physical location of a voxel and the tensor at that location under the reasoning that voxels belonging to a nucleus would be close in physical

proximity and in tensor properties. The overall dimensionless E_{jk} was defined as the normalized sum of the Mahalanobis norm and the J-Divergence [50].

$$E_{jk} = \sqrt{\left(x_j - \bar{x}_k\right)^T W_k^{-1}\left(x_j - \bar{x}_k\right)} + \sqrt{tr\left(\boldsymbol{D}_j{}^{-1}\bar{\boldsymbol{D}}_k + \bar{\boldsymbol{D}}_k{}^{-1}\boldsymbol{D}_j\right) - 2a}$$

$\boldsymbol{x}_j$ is the three-dimensional coordinate vector of voxel *j*, $\bar{\boldsymbol{x}}_k$ represents the coordinate vector of the centroid of cluster *k*, W_k is the covariance matrix of cluster *k* (recalculated at every iteration), $\boldsymbol{D}_j$ is the corresponding diffusion tensor of voxel *j*, $\bar{\boldsymbol{D}}_k$ is the mean diffusion tensor for the centroid of cluster *k*, and *a* is the size of the tensors (a = 3). The combination of metrics for physical proximity and tensor similarity follow logically from the observation that voxels within thalamic nuclei are near one another and have similar diffusivity (and therefore conductivity) tensor properties. The algorithm calculates the distance metric between each cluster's centroid and all voxels. Voxels are assigned to a cluster by minimization of voxel-to-cluster centroid distance, and this process repeats until the convergence criterion is satisfied. Like Wiegell et al. [15], we defined the stopping point of the algorithm as the point at which no cluster centroid shifted more than 0.1 mm from the previous iteration.

3.2.3.3 Centroid Comparison

Centroid coordinates of the patient segmented nuclei were pooled across subjects (N = 10); the Wakana DTI atlas thalamus was evaluated separately [51]. The Y-coordinates were scaled by the AC-PC length to partially adjust for inter-subject variability. Unlike previous centroid for thalamic k-means segmentation [15, 48], we did not register the segmentations to a normalized atlas. As in previously published work [48], we compared the three-dimensional centroid coordinates of each segmented nucleus with atlas coordinates obtained from the Morel

histological atlas [47]. We also calculated the distance of the centroid coordinates of the segmented nuclei from the posterior commissure (PC) and compared those values against calculated values from the Morel histological atlas with two-tailed t-tests at a significance level of $p < 0.05$.

3.2.3.4 Position of DBS Leads

The distances between VLPv centroids and the electrode contacts that best controlled tremor were calculated in patient and atlas space.

3.2.4 Atlas-based data

The DTI atlas is described in [51]. A single-shot echo planar imaging sequence was used to acquire the atlas with a b-value of 700 s/mm^2 and a 2.2 mm isotropic voxel size. The left thalamus was already parcellated by hand as described in [32]. The atlas thalamus [51] was segmented with our k-means clustering algorithm. Cicerone [52] provided stereotactic electrode coordinates in atlas space.

3.2.5 VTA Analysis

The VTA is an estimate of the region(s) of the brain that fires action potentials under a given set of stimulation parameters [32]. We generated the VTAs for clinically efficacious stimulation settings and characterized their overlaps with relevant anatomy.

All simulations were performed on a custom-built computer with 8 processors and 48 GB memory (DEH Microsystems LLC, Cleveland, OH, USA) using BioPSE (Scientific Computing and Imaging Institute, University of Utah, Salt Lake City, UT).

3.2.5.1 VTA Generation

For each patient, individualized and atlas-based VTAs were generated. The individualized model followed the methodology of the atlas-based model presented in [29, 32, 53, 54] with the exception that all brain tissue conductivity data was based on patient-specific DTI data, and not derived from the Wakana et al. (2004) DTI atlas [51] as in all previous VTA studies. To briefly describe the VTA calculation process, a Fourier FEM Solver first solves the Poisson equation to determine voltage as a function of time and space within the patient's brain tissue. The voltage solution is dependent upon several factors, including where the electrode is placed in the brain, the patient's brain conductivity at the voxel level nearest to the electrode contacts, the stimulation settings being modeled, and the electrode-tissue interface (electrode capacitance and impedance). The VTA is defined as the region(s) for which the second spatial derivative of the extracellular potential distribution [55, 56] exceeds an axonal activation threshold derived from NEURON [57] modeling [29, 32].

For VTA modeling, stimulation settings were selected from each patient's first stimulation programming session with a Neurologist (KLC) following the post-operative CT scan, 6-8 weeks post-DBS surgery. We recorded the optimal DBS setting that controlled tremor without producing side-effects.

3.2.5.2 VTA Evaluation

For each stimulation setting, the overlap volumes between the VTA and the motor thalamus (VLPv, VLPd, VLa) sensory thalamus (VPM and VPL), and the internal capsule (IC, lateral to the thalamus) were recorded with the individualized and atlas-based models. Overall agreement in VTA volumes between the two models was assessed with a two-tailed paired t-test.

3.2.6 Statistical Methods

Statistical analysis was performed using commercially available software: Excel (Microsoft Inc., Redmond, WA) and MATLAB (Mathworks, Natick, MA). For all comparisons, statistical significance is defined at the $p < .05$ level, and a statistical trend is defined as $0.05 < p < 0.10$. Sources of statistical variability in our data include quantization effects due to voxel representation intrinsic to MR imaging, motion artifacts in MR and CT imaging, and human error in measurement [40]. Data are displayed as mean ± SD except where otherwise noted.

3.3 Results

3.3.1 Clinical Outcome

All 10 patients had improved tremor following successful DBS surgery, without sustained paresthesias or dysarthria.

3.3.2 Thalamic Segmentation

Representative cross-sectional images of segmented thalami are shown with corresponding atlas images [47] and 3T MR images in Figure 3-1. The representative images demonstrate that there is good agreement in the location and size of the thalamic nuclei between our results and the Morel atlas, though there is variability in the overall size of the thalamus and locations of the thalamic nuclei boundaries across patients (Fig. 3-2).

The repeatability of the k-means algorithm was tested on the Wakana DTI atlas thalamus before applying the algorithm to individual patient thalami. We attempted 10 segmentations with randomized initial centroid coordinates within a

radius of 3 mm of the initial centroid coordinates used for the segmentation in VTA modeling. We calculated the average deviation of the nuclei centroids from the best segmentation's centroids and pooled them across iterations (N = 10).

We quantitatively compared our results to the Morel Atlas. After scaling the anteroposterior coordinates by the AC-PC length (patient mean ± SD AC-PC length = 25.8 ± 1.9 mm, Morel atlas, postmortem AC-PC length = 24 mm) to partially account for variation from the atlas thalamus, the average absolute Euclidean distance difference between the average centroids and the Morel centroids is 4.0 mm. The Euclidean distance difference is 2.2 mm in the mediolateral axis, 2.6 mm in the anteroposterior axis, and 0.8 mm in the dorsoventral axis. Two-tailed t-tests reveal that the A, VA, VLa, VLPd, VLPv, VPL, VPM, P, and CM nuclei coordinates are not significantly different ($p >> 0.05$) in absolute Euclidean distance from the PC compared to Morel atlas coordinates, suggesting good agreement with atlas values. Only MD, LD, LP, and VM nuclei centroid coordinates are significantly different ($p < 0.05$). The algorithm produced repeatable results on a standardized atlas thalamus; on average, when initial centroid coordinates were randomized to a 3 mm radius, the segmentation yielded nuclei centroid 1.35 ± 0.84 mm from the centroids belonging to the best segmentation (i.e., the one used for atlas-based VTA analysis).

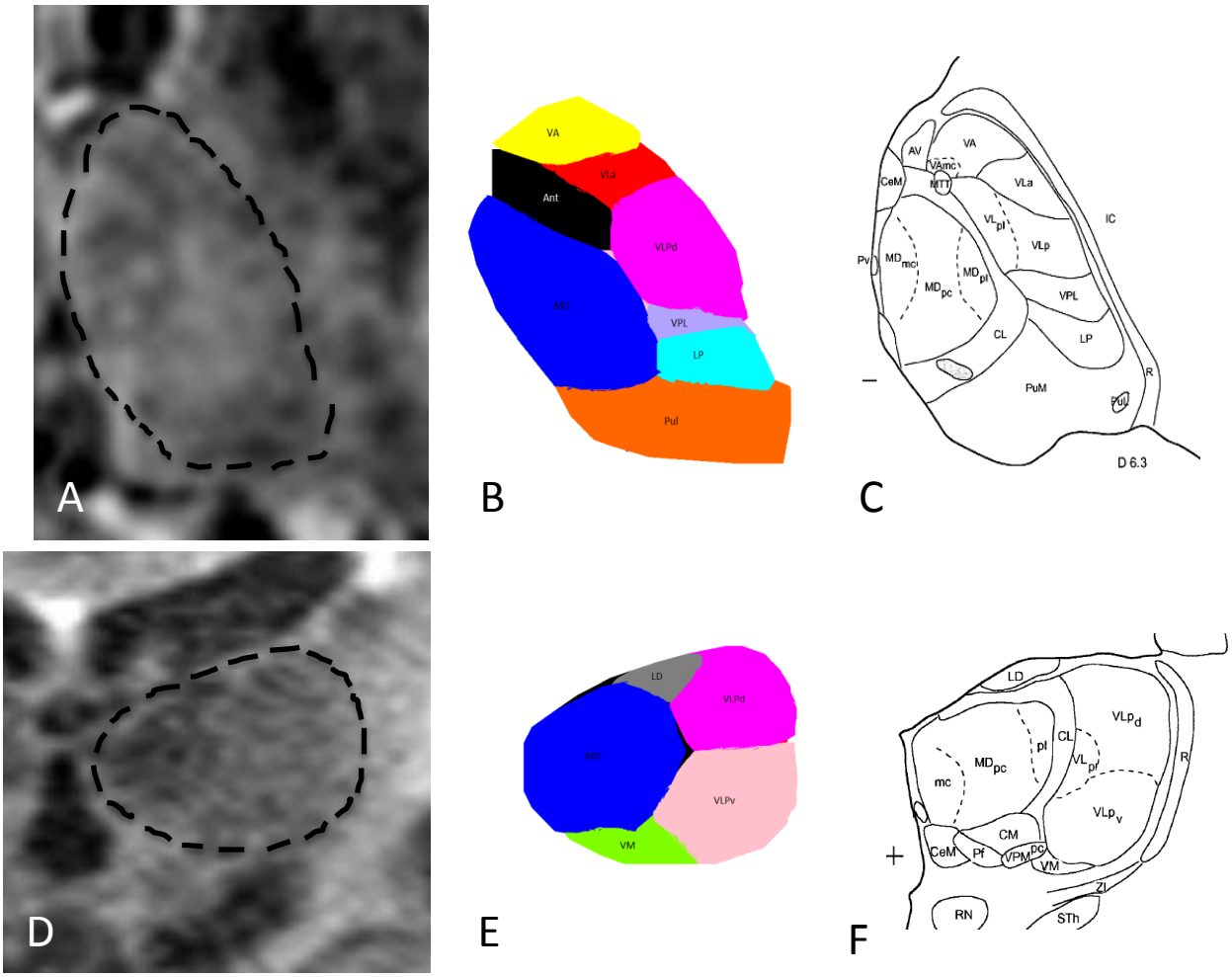

Figure 3-1. Comparison of patient segmentations with corresponding MR images and Morel histological atlas renderings. [47] Atlas renderings were reprinted with permission from Wiley. The borders of the thalamus are indicated by the dotted line (A and D).

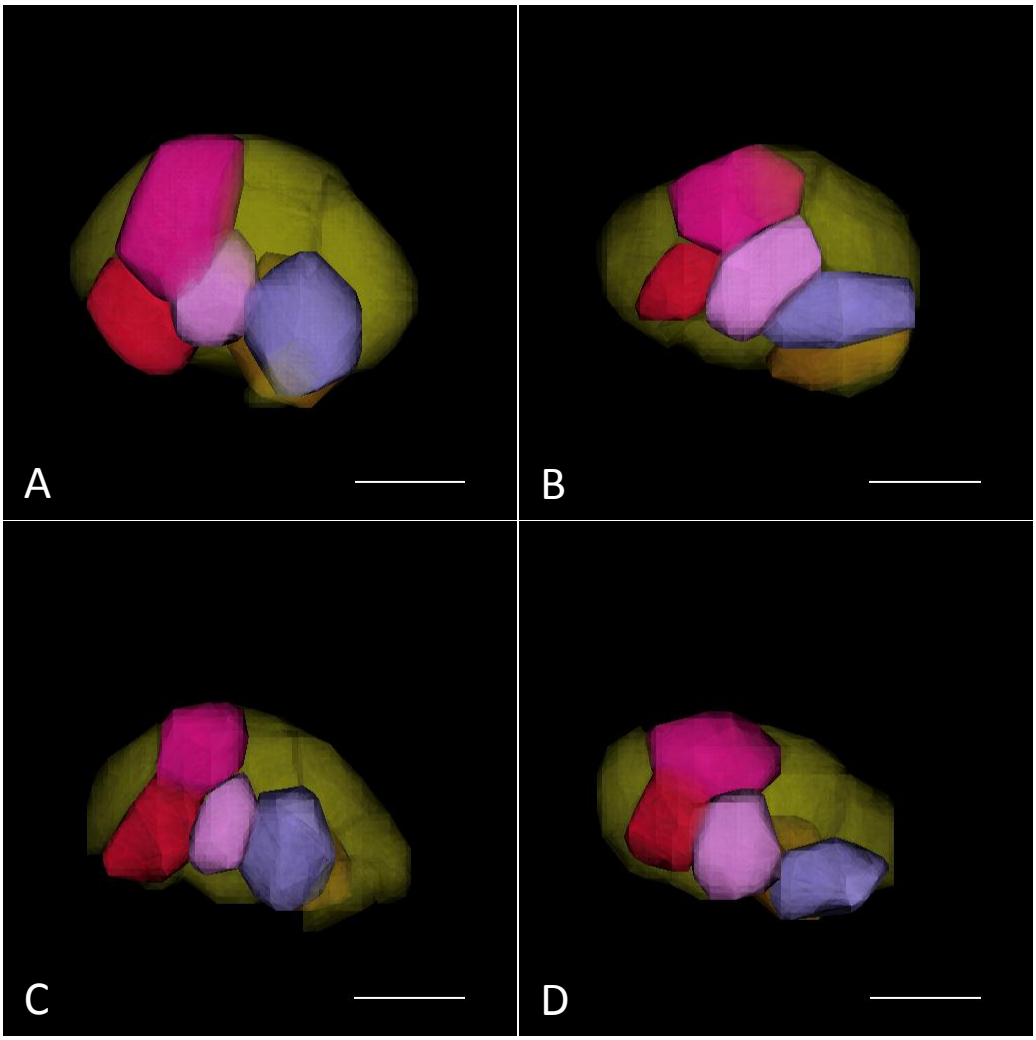

Figure 3-2. Comparison of sagittal projections of segmented thalami. The k-means algorithm accommodates different thalamus shapes and sizes. (A) Wakana DTI atlas thalamus (B, C, D) 3 ET patient thalami. Scale bars represent 10 mm. (key: crimson = VLa, magenta = VLPd, pink = VLPv, purple = VPL, brown = VPM)

3.3.3 Location of DBS Active Contacts

3.3.3.1 Individual Patient Analysis

70% of the most efficacious contacts lie within the motor (VL) nucleus. On average, the Final DBS active contact is 1.8 mm medial ,1.2 mm anterior, and 0.8 mm superior to the VLPv centroid (overall distance: 4.6 ± 1.7 mm). When compared with a paired two-tailed t-test, there is a significant difference in location

between the VLPv centroids' and the active contacts' mediolateral coordinates ($p < 0.05$). However, there is no difference in the anteroposterior and dorsoventral coordinates ($p > 0.05$) between each patient's VLPv centroids and the active contacts, indicating that the Y and Z coordinates of the optimal stimulation site are well-predicted with the k-means clustering algorithm's definition of the VLPv centroid. Consistent with typical lead placements in ET DBS, the mean Final DBS Active Contact is 14.0 mm lateral, 7.5 mm anterior, and 4.6 mm superior to the PC [9, 39]. On average, the Distal Tip of the electrode is placed 0.5 mm medial, 1.0 mm posterior, and 0.8 mm inferior to the VIM target defined by the S-W atlas.

3.3.3.2 Atlas-Based Analysis

60% of the most efficacious contacts lie within the motor nucleus. On average, the Final DBS active contact is at the medial, 0.7 mm posterior to, and 2.7 mm superior to the VLPv centroid (overall distance: 5.0 ± 2.9 mm). When compared with a paired two-tailed t-test, there is no significant difference in location between the VLPv centroids' and the active contacts' mediolateral, anteroposterior, or dorsoventral coordinates ($p > 0.05$).

Our data indicates a statistical trend (F-test, $p = 0.07$) towards a difference in variance between individualized and atlas-based models (3.1 mm^2 and 8.7 mm^2, respectively).

3.3.4 Comparison of Individualized and Atlas-Based VTAs

Paired t-tests show that there is no statistically significant difference between VTAs generated by individualized and atlas-based modeling ($p = 0.18$). The mean percentage difference between individualized and atlas-based VTAs is 6.82% ± 13.1%. 100% of individualized VTAs of the most efficacious tremor control settings for each patient overlap with the motor thalamus, while only 90% of equivalent atlas-based VTAs overlap with the motor thalamus. More specifically, 90% of individualized VTAs have some overlap with the VLPv, while the remaining 10% overlap with the VLPd. In atlas-based modeling, 70% of VTAs have some overlap with the VLPv, while 20% overlap with the VLPd and 10% are entirely medial to the motor thalamus. There is no statistically significant difference in the volume of VLPv stimulation or sensory thalamus stimulation between models ($p = 0.58$ and $p = 0.94$, respectively).

Figure 3-3 shows four examples of individualized VTAs for the most clinically-efficacious tremor control setting. In all examples, the VTA lies primarily within the motor thalamus, as is expected for effective tremor control. The VLPd (magenta) appears to be an effective location for tremor control in addition to the VLPv (pink). Figure 3-4 shows two examples of patients whose individualized model better predicts VTA position than the atlas-based model. In both cases, individualized modeling predicts a VTA overlapping mostly with the motor thalamus, while the atlas-based model places the VTA entirely medial (Fig. 3-4A) or mostly posterior (Fig. 3-4C) to the motor thalamus.

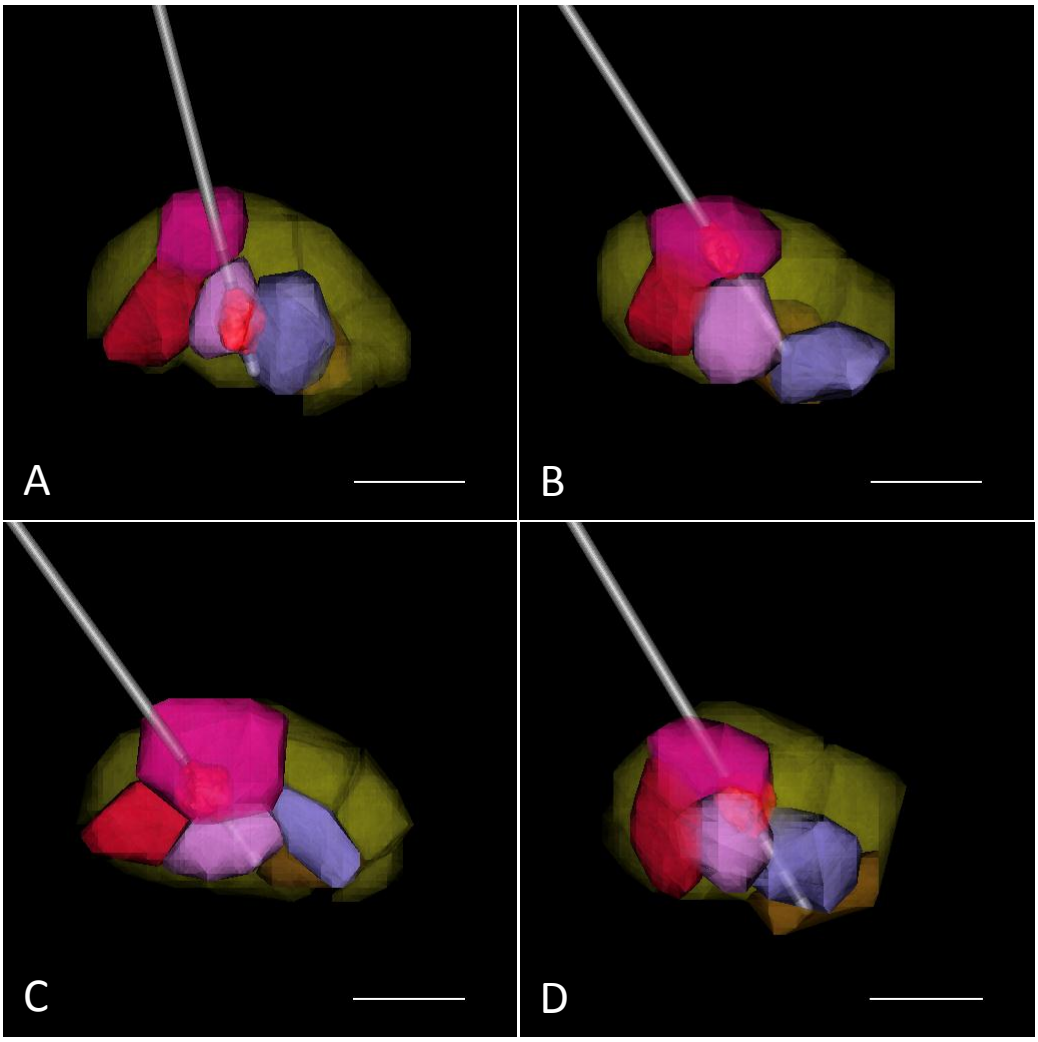

Figure 3-3. Examples of VTAs of the most efficacious tremor control settings for four patients. In all examples, the VTA lies primarily within the motor thalamus. Scale bars represent 10 mm. (key: crimson = VLa, magenta = VLPd, pink = VLPv, purple = VPL, brown = VPM, red = VTA)

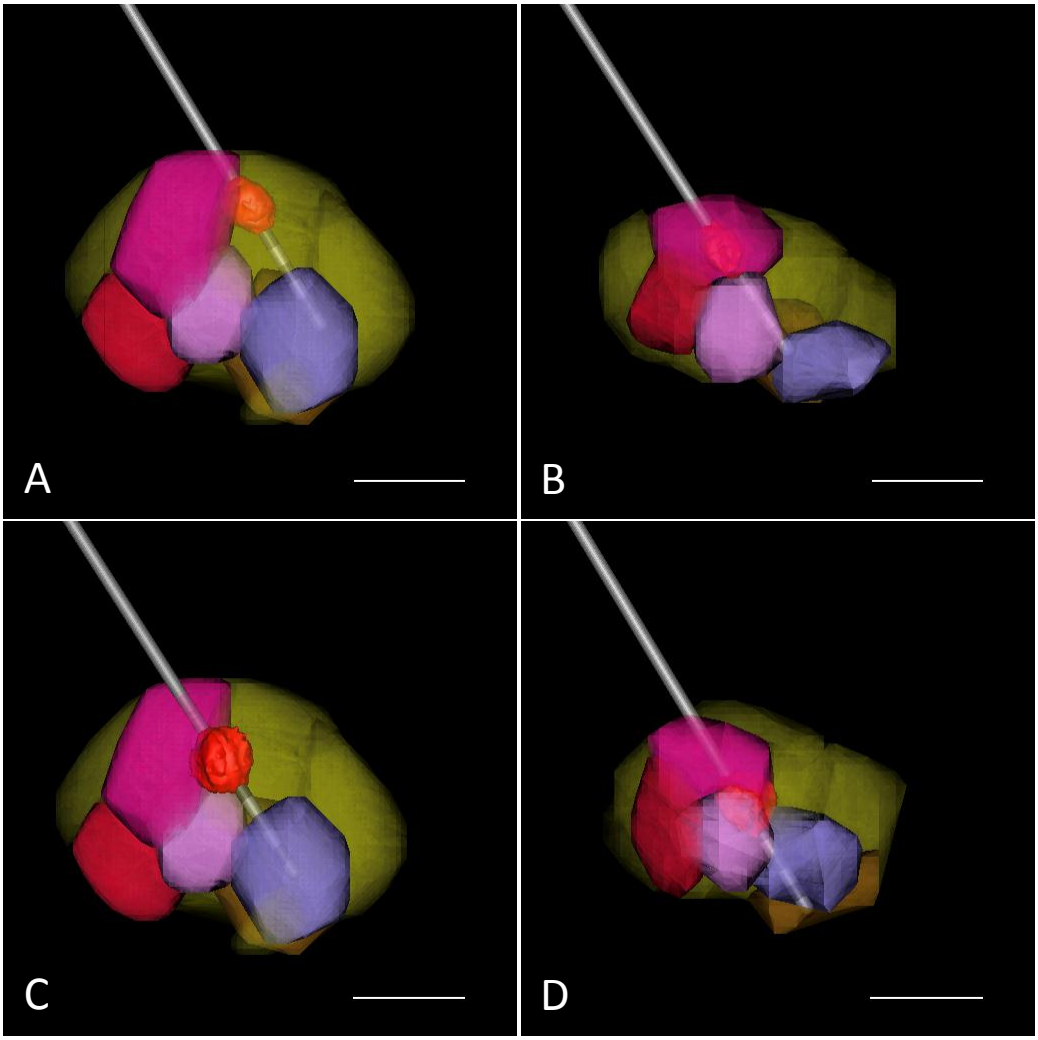

Figure 3-4. Comparison of Atlas-based and Individualized VTA modeling during tremor control. (A) Atlas-based modeling shows a VTA during tremor control (monopolar stimulation, C+3-, 1V) that lies mostly posteromedial to the motor thalamus. (B) Individualized modeling of the same stimulation setting shows the VTA situated within the motor thalamus. (C) Atlas-based modeling shows a VTA during tremor control (monopolar stimulation, C+3-, 1.5V) that the VTA lies mostly posterior to the motor thalamus. (D) Individualized modeling of the same stimulation setting shows the VTA almost entirely within the motor thalamus. Scale bars represent 10 mm. (key: crimson = VLa, magenta = VLPd, pink = VLPv, purple = VPL, brown = VPM, red = VTA)

3.4 Discussion

The purpose of this study is to introduce an individualized VTA model of thalamic DBS. We generated atlas-based and individualized VTAs for optimal tremor control settings in segmented thalami and compared the results. Until now, investigation of VTAs in thalamic DBS has been difficult due to the inability to visualize the functionally-distinct nuclei of the thalamus. To overcome this difficulty, we applied a k-means clustering algorithm on DTI data, and integrated the results into a finite-element electric field DBS model. Ours is the first study to model ET DBS VTAs and the first to model VTAs in an individualized manner (i.e., without the use of atlas-based anatomy or tissue conductivity).

3.4.1 Previous Work

Previous computational investigations of ET DBS relied on common brain-spaces or co-registering patient data to brain atlases to analyze data across patients [37-39]. One retrospective DBS study [39] applied probabilistic diffusion tractography [18] within Montreal Neurological Institute (MNI) brain space to analyze the connectivity between the most efficacious DBS contact for tremor control and prefrontal, premotor, and primary motor cortical target masks. Pouratian et al. hypothesized that the most efficacious DBS contact for tremor control would co-localize with the region in the thalamus with most primary motor cortex connectivity, but instead, the contact is typically anterior to that region in an area with high likelihood of connectivity with the premotor and supplementary motor cortices. A recent retrospective ET DBS study investigated the potential for improved modulation of neuronal pathways with directional DBS leads using finite-element electric field modeling. However, the study utilized an isotropic

homogeneous medium for its tissue conductivity model and warped thalamic atlas nuclei to patient data in place of individual segmentation [38].

3.4.2 Thalamic Segmentation

Though the functionally-distinct nuclei of the thalamus are not visible on conventional MRI, DTI data can help delineate thalamic nuclei [13, 14, 16]. We modified a k-means clustering algorithm previously published by Wiegell et al. (2003) [15] for semi-automatic thalamic segmentation for use in retrospectively evaluating clinical data. Wiegell's k-means clustering algorithm utilized diffusivity tensor data to semi-automatically segment the thalamus into a pre-defined number of clusters. Our algorithm differed in two ways. First, we used conductivity--not diffusivity--tensors for segmentation. Tuch et al. (2001) demonstrated that the relationship between conductivity and diffusivity is linear [45]. Therefore, there should be no difference in segmentation from using conductivity tensors over diffusivity tensors. Secondly, though Wiegell et al. (2003) obtained good results by using the Frobenius norm as a tensor dissimilarity metric, we used the square root of the J-Divergence, or the symmetrized Kullback-Leibler divergence [50] to overcome some of the limitations of the Frobenius norm. Unlike the Frobenius norm, the J-divergence is both affine-invariant and inherently considers the positive-definite quality of tensors [58]. The motion of water within brain tissue over time t is represented by a Gaussian distribution, and diffusion tensors are equivalent to the covariance matrix of the Gaussian distribution. It is therefore reasonable to treat the distance between tensors as the distance between that Gaussian distribution [50, 58].

We tested the robustness of the algorithm on a standardized atlas thalamus, and then applied the algorithm to patient thalami. We were able to semi-automatically

segment the thalamus on a patient-specific basis using conductivity tensor data already required for VTA modeling. The algorithm run time was less than 10 minutes following approximately 3 hours of data pre-processing per patient. As in previous studies, we felt that placement of the initial centroids for the k-means algorithm with *a priori* knowledge of atlas centroid coordinates was justified [48] as it dramatically reduced the runtime of the algorithm and provided better segmentation results (comparison not shown). Our segmentation results are comparable to previously-published k-means thalamic segmentation algorithms, despite the fact that previous studies co-registered segmentation results to the Morel atlas prior to comparing the nuclei centroids, naturally biasing the result [15, 48]. Deoni et al. reported an absolute Euclidean distance difference between their segmented nuclei's centroids and Morel atlas centroids of 3.3 mm, and in the orthogonal axes, differences of 2.2 mm (mediolateral), 1.7 mm (anteroposterior), and 1.3 mm (dorsoventral) [48]. Our segmentation is equivalent in the mediolateral axis, superior in the dorsoventral axis, but inferior in the anteroposterior axis even without atlas co-registration. However, it is not entirely reasonable to treat atlas nuclei centroid coordinates as gold standards for comparison; variation is expected in nuclei location and boundaries across patients, and recent tractography studies reveal substantial variability across patient thalamic nuclei [17, 18]. Post-mortem histological staining is currently the only reliable method for assessing the boundaries of thalamic nuclei, though this approach would likely require a multi-institutional longitudinal study. Pre-operatively, however, if there were a way to confirm the results of semi-automated thalamic segmentation, that method would likely be used for targeting.

3.4.3 Position of DBS Leads

The position of the DBS leads within the segmented thalami suggests that the segmentation is reasonable in both an atlas thalamus and across patient thalami. On a patient-specific basis, the segmentation algorithm can predict the DBS active contact coordinates in the anteroposterior and dorsoventral axes. The inability of the algorithm to predict the mediolateral coordinate of the DBS active contact is expected, because the centroid of the VLPv is not typically the target for ET DBS due to the somatotopic organization of the thalamus. As our data shows, the active contact is typically medial to the VLPv centroid. This result lends credibility to the k-means algorithm as a potential method for surgical planning.

Previous studies have argued in favor of selecting targeting methods with superior precision [59, 60]. When compared to Cicerone-based electrode placement, there is an interesting though not statistically significant difference in the variability of VLPv centroid to active contact distance. The lack of statistical significance is likely due to the relatively small sample size of our study. Coordinate-based lead location has been shown to not be a significant predictor of clinical outcome in Parkinson's Disease [61]; VTAs may be better predictors.

3.4.4 VTA Analysis

Though there is no statistically significant difference in VTA size between models, there is high variability in VTA size between models due to differences in lead location within the thalamus. In cases with clear disagreement between electrode locations between models, the surrounding tissue conductivity may contribute to large differences in VTA size. Atlas-based VTA modeling performs generally well, though our preliminary results suggest that individualized VTA modeling may perform better in some instances.

3.4.5 Limitations and Future Directions

Because this study was retrospective, we used a thalamic segmentation method that utilized data from existing imaging data. There is potential for improving upon this thalamic segmentation method in the future with higher-resolution DTI scans or alternative statistical clustering approaches. Also, the small sample size of this study (N = 10) likely prevents finding statistical significance in some of our comparisons.

In an accompanying study, we use this methodology to correlate side-effects of DBS to VTA stimulation in the thalamus for the same patients. We hope to validate our methodology and implement it in DBS surgical planning in a prospective study.

3.5 Conclusions

We have presented the first individualized VTA model for ET DBS patients. Compared to traditional stereotactic targeting of the VLPv, DTI-based thalamic segmentation may be a superior method for locating the centroid of the VLPv. Preliminary VTA modeling results indicate that clinical effects may be better explained with individualized modeling than by traditional atlas-based modeling. We explore this further in an accompanying study.

3.6 References

1. Gardner, D., et al., Terminology for neuroscience data discovery: multi-tree syntax and investigator-derived semantics. Neuroinformatics, 2008. **6**(3): p. 161-74.

2. Macchi, G. and E.G. Jones, Toward an agreement on terminology of nuclear and subnuclear divisions of the motor thalamus. J Neurosurg, 1997. **86**(1): p. 77-92.

3. Ehlen, F., et al., Differential effects of deep brain stimulation on verbal fluency. Brain and Language, 2014. **134**(0): p. 23-33.

4. Vaillancourt, D.E., et al., Deep brain stimulation of the VIM thalamic nucleus modifies several features of essential tremor. Neurology, 2003. **61**(7): p. 919-25.

5. Benabid, A.L., et al., Chronic electrical stimulation of the ventralis intermedius nucleus of the thalamus as a treatment of movement disorders. J Neurosurg, 1996. **84**(2): p. 203-14.

6. Koller, W., et al., High-frequency unilateral thalamic stimulation in the treatment of essential and parkinsonian tremor. Ann Neurol, 1997. **42**(3): p. 292-9.

7. Koller, W.C., et al., Long-term safety and efficacy of unilateral deep brain stimulation of the thalamus in essential tremor. Mov Disord, 2001. **16**(3): p. 464-8.

8. Kumar, R., et al., Long-term follow-up of thalamic deep brain stimulation for essential and parkinsonian tremor. Neurology, 2003. **61**(11): p. 1601-4.

9. Klein, J.C., et al., The tremor network targeted by successful VIM deep brain stimulation in humans. Neurology, 2012. **78**(11): p. 787-95.

10. Vitek, J.L., Mechanisms of deep brain stimulation: excitation or inhibition. Mov Disord, 2002. **17 Suppl 3**: p. S69-72.

11. McIntyre, C.C., et al., Uncovering the mechanism(s) of action of deep brain stimulation: activation, inhibition, or both. Clin Neurophysiol, 2004. **115**(6): p. 1239-48.

12. Montgomery, E.B., Jr. and J.T. Gale, Mechanisms of action of deep brain stimulation(DBS). Neurosci Biobehav Rev, 2008. **32**(3): p. 388-407.

13. Wiegell, M.R., H.B. Larsson, and V.J. Wedeen. Diffusion tensor MRI of the thalamus: differentiation of nuclei by their projections. in Proceedings of the International Society for Magnetic Resonance in Medicine. 1999.

14. Wiegell, M.R., et al. Automatic identification of thalamic nuclei from DTI. in Proceedings of the Sixth International Conference on Functional Mapping of the Human Brain. 2000.

15. Wiegell, M.R., et al., Automatic segmentation of thalamic nuclei from diffusion tensor magnetic resonance imaging. Neuroimage, 2003. **19**(2 Pt 1): p. 391-401.

16. Niemann, K., et al., The Morel stereotactic atlas of the human thalamus: atlas-to-MR registration of internally consistent canonical model. Neuroimage, 2000. **12**(6): p. 601-16.

17. Johansen-Berg, H., et al., Functional-anatomical validation and individual variation of diffusion tractography-based segmentation of the human thalamus. Cereb Cortex, 2005. **15**(1): p. 31-9.

18. Behrens, T.E., et al., Non-invasive mapping of connections between human thalamus and cortex using diffusion imaging. Nat Neurosci, 2003. **6**(7): p. 750-7.

19. Duan, Y., et al., Thalamus segmentation from diffusion tensor magnetic resonance imaging. Conf Proc IEEE Eng Med Biol Soc, 2006. **1**: p. 3628-31.

20. Grassi, A., et al., Thalamic nuclei clustering on High Angular Resolution Diffusion Images, in International Society for Magnetic Resonance in Medicine. 2008: Toronto.

21. Jonasson, L., et al., A level set method for segmentation of the thalamus and its nuclei in DT-MRI. Signal Processing, 2007. **87**: p. 309-321.

22. Mang, S.C., et al., Thalamus segmentation based on the local diffusion direction: a group study. Magn Reson Med, 2012. **67**(1): p. 118-26.

23. Rittner, L., et al. Segmentation of thalamic nuclei based on tensorial morphological gradient of diffusion tensor fields. in Biomedical Imaging: From Nano to Macro, 2010 IEEE International Symposium on. 2010.

24. Schultz, T., Segmenting Thalamic Nuclei: What Can We Gain from HARDI?, in Medical Image Computing and Computer-Assisted Intervention – MICCAI 2011, G. Fichtinger, A. Martel, and T. Peters, Editors. 2011, Springer Berlin Heidelberg. p. 141-148.

25. Ziyan, U., D. Tuch, and C.F. Westin, Segmentation of thalamic nuclei from DTI using spectral clustering. Med Image Comput Comput Assist Interv, 2006. **9**(Pt 2): p. 807-14.

26. Ziyan, U. and C.F. Westin, Joint segmentation of thalamic nuclei from a population of diffusion tensor MR images. Med Image Comput Comput Assist Interv, 2008. **11**(Pt 1): p. 279-86.

27. Barkhoudarian, G., et al., A role of diffusion tensor imaging in movement disorder surgery. Acta Neurochir (Wien), 2010. **152**(12): p. 2089-95.

28. Benabid, A.L., Deep brain stimulation for Parkinson's disease. Curr Opin Neurobiol, 2003. **13**(6): p. 696-706.

29. Butson, C.R., et al., Predicting the effects of deep brain stimulation with diffusion tensor based electric field models. Med Image Comput Comput Assist Interv, 2006. **9**(Pt 2): p. 429-37.

30. Miocinovic, S., et al., Computational analysis of subthalamic nucleus and lenticular fasciculus activation during therapeutic deep brain stimulation. J Neurophysiol, 2006. **96**(3): p. 1569-80.

31. Chaturvedi, A., et al., Subthalamic nucleus deep brain stimulation: accurate axonal threshold prediction with diffusion tensor based electric field models. Conf Proc IEEE Eng Med Biol Soc, 2006. **1**: p. 1240-3.

32. Butson, C.R., et al., Patient-specific analysis of the volume of tissue activated during deep brain stimulation. Neuroimage, 2007. **34**(2): p. 661-70.

33. Butson, C.R. and C.C. McIntyre, Current steering to control the volume of tissue activated during deep brain stimulation. Brain Stimul, 2008. **1**(1): p. 7-15.

34. Maks, C.B., et al., Deep brain stimulation activation volumes and their association with neurophysiological mapping and therapeutic outcomes. J Neurol Neurosurg Psychiatry, 2009. **80**(6): p. 659-66.

35. Chaturvedi, A., et al., Patient-specific models of deep brain stimulation: influence of field model complexity on neural activation predictions. Brain Stimul, 2010. **3**(2): p. 65-7.

36. Butson, C.R., et al., Probabilistic analysis of activation volumes generated during deep brain stimulation. Neuroimage, 2011. **54**(3): p. 2096-104.

37. Kuncel, A.M., S.E. Cooper, and W.M. Grill, A method to estimate the spatial extent of activation in thalamic deep brain stimulation. Clin Neurophysiol, 2008. **119**(9): p. 2148-58.

38. Keane, M., et al., Improved spatial targeting with directionally segmented deep brain stimulation leads for treating essential tremor. J Neural Eng, 2012. **9**(4): p. 046005.

39. Pouratian, N., et al., Multi-institutional evaluation of deep brain stimulation targeting using probabilistic connectivity-based thalamic segmentation. J Neurosurg, 2011. **115**(5): p. 995-1004.

40. Patil, P.G., et al., The anatomical and electrophysiological subthalamic nucleus visualized by 3-T magnetic resonance imaging. Neurosurgery, 2012. **71**(6): p. 1089-95; discussion 1095.

41. Studholme, C., D.J. Hawkes, and D.L. Hill. Normalized entropy measure for multimodality image alignment. 1998.

42. Aberth, O., The Transformation of Tensors into Diagonal Form. SIAM Journal on Applied Mathematics, 1967. **15**(5): p. 1247-1252.

43. Alexander, A.L., et al., Diffusion Tensor Imaging of the Brain. Neurotherapeutics : the journal of the American Society for Experimental NeuroTherapeutics, 2007. **4**(3): p. 316-329.

44. Alexander, D.C., et al., Spatial transformations of diffusion tensor magnetic resonance images. IEEE Trans Med Imaging, 2001. **20**(11): p. 1131-9.

45. Tuch, D.S., et al., Conductivity tensor mapping of the human brain using diffusion tensor MRI. Proc Natl Acad Sci U S A, 2001. **98**(20): p. 11697-701.

46. Haueisen, J., et al., The influence of brain tissue anisotropy on human EEG and MEG. Neuroimage, 2002. **15**(1): p. 159-66.

47. Morel, A., M. Magnin, and D. Jeanmonod, Multiarchitectonic and Stereotactic Atlas of the Human Thalamus. The Journal of Comparative Neurology, 1997. **3877**: p. 588-630.

48. Deoni, S.C., et al., Segmentation of thalamic nuclei using a modified k-means clustering algorithm and high-resolution quantitative magnetic resonance imaging at 1.5 T. Neuroimage, 2007. **34**(1): p. 117-26.

49. Hartigan, J.A.W., M. A., A K-Means Clustering Algorithm. Journal of the Royal Statistical Society. Series C (Applied Statistics), 1979. **28**(1): p. 100-108.

50. Wang, Z. and B.C. Vemuri, DTI segmentation using an information theoretic tensor dissimilarity measure. IEEE Trans Med Imaging, 2005. **24**(10): p. 1267-77.

51. Wakana, S., et al., Fiber tract-based atlas of human white matter anatomy. Radiology, 2004. **230**(1): p. 77-87.

52. Miocinovic, S., et al., Cicerone: stereotactic neurophysiological recording and deep brain stimulation electrode placement software system. Acta Neurochir Suppl, 2007. **97**(Pt 2): p. 561-7.

53. Butson, C.R. and C.C. McIntyre, Tissue and electrode capacitance reduce neural activation volumes during deep brain stimulation. Clin Neurophysiol, 2005. **116**(10): p. 2490-500.

54. McIntyre, C.C., et al., Electric field and stimulating influence generated by deep brain stimulation of the subthalamic nucleus. Clinical Neurophysiology, 2004. **115**(3): p. 589-595.

55. Rattay, F., Analysis of Models for External Stimulation of Axons. Biomedical Engineering, IEEE Transactions on, 1986. **BME-33**(10): p. 974-977.

56. McNeal, D.R., Analysis of a Model for Excitation of Myelinated Nerve. Biomedical Engineering, IEEE Transactions on, 1976. **BME-23**(4): p. 329-337.

57. Hines, M.L. and N.T. Carnevale, The NEURON simulation environment. Neural Comput, 1997. **9**(6): p. 1179-209.

58. DaSilva, A.F., et al., A primer on diffusion tensor imaging of anatomical substructures. Neurosurg Focus, 2003. **15**(1): p. E4.

59. Andrade-Souza, Y.M., et al., Comparison of three methods of targeting the subthalamic nucleus for chronic stimulation in Parkinson's disease. Neurosurgery, 2005. **56**(4): p. 360-368.

60. Houshmand, L., et al., Evaluating Indirect Subthalamic Nucleus Targeting with Validated 3-Tesla Magnetic Resonance Imaging. Stereotact Funct Neurosurg, 2014. **92**(6): p. 337-345.

61. Nestor, K.A., et al., Coordinate-based lead location does not predict Parkinson's disease deep brain stimulation outcome. PLoS One, 2014. **9**(4): p. e93524.

Chapter 4

Investigation of Side Effects in Thalamic Deep Brain Stimulation with Individualized and Atlas-Based Volume of Tissue Activated Modeling

Abstract

Background/Aims: Volume of Tissue Activated (VTA) modeling has improved the understanding of deep brain stimulation (DBS) surgery for movement disorders. In a previous work, we described the development of an individualized VTA model for thalamic DBS for Essential Tremor (ET). Preliminary results indicated that individualized VTA modeling may confer some advantages over existing atlas-based modeling. We sought to investigate the potential for individualized and atlas-based VTA modeling to accurately predict the most common DBS side effects (sustained paresthesias and dysarthria) in patients with well-positioned DBS leads.

Methods: We utilized the VTA modeling methodologies presented in Chapter 3. VTAs of efficacious and side effect-inducing settings were calculated for $N = 10$ ET patients who had undergone left thalamic DBS. We compared VTA overlap volumes with relevant anatomy (motor thalamus, sensory thalamus, internal

capsule) and correlated them to observed clinical effects (tremor control, sustained sensory paresthesias, dysarthria/speech side-effects).

Results: Individualized VTA predicts dysarthria resulting from internal capsule (IC) stimulation (Barnard's Exact test, $p < 0.05$) whereas atlas-based VTA modeling does not (Barnard's Exact test, $p > 0.05$). There is no statistically significant difference in sensory thalamus stimulation between models during sustained sensory paresthesias (paired t-test, $p > 0.05$). The incidence of sustained sensory paresthesias on proximal contacts (2 and 3) indicates that paresthesias may result from stimulation outside of the sensory thalamus.

Conclusions: Individualized VTA modeling may confer some advantages over traditional atlas-based approaches. Our results present an opportunity for improved DBS planning.

Abbreviations: **DBS**, deep brain stimulation; **ET**, Essential Tremor; **VTA**, Volume of Tissue Activated; **Vim**, Ventral Intermediate; **Vc**, Ventrocaudal; **MRI**, Magnetic Resonance Imaging; **DTI**, Diffusion Tensor Imaging; **VLPd**, Ventral Lateral Posterior-dorsal ; **VLPv**, Ventral Lateral Posterior-ventral; **VPL**, Ventral Posterior Lateral; **VPM**, Ventral Posterior Medial; **IC**, Internal Capsule.

4.1. Introduction

Thalamic deep brain stimulation (DBS) effectively controls medically-refractory kinetic and postural tremor in Essential Tremor (ET) [1-5]. Despite its efficacy, the mechanism of DBS remains controversial [6-8]. Thalamic DBS is especially difficult to study due to the inability to visualize the functionally-distinct nuclei of the thalamus [5].

Modeling the volume of tissue activated (VTA) in DBS has been used to investigate the impact of stimulation parameters on clinical outcome in Parkinson's disease (PD) DBS [9-16], though these studies rely on common brain-spaces for modeling. In our accompanying study, we presented an individualized VTA model for ET DBS and a preliminary comparison to traditional atlas-based VTA modeling. Using the methods presented in Chapter 3, we investigated the ability of individualized and atlas-based VTA models to explain common side effects from DBS in ET patients with well-positioned leads.

During stimulation programming, ET patients typically experience side effects. While some side effects are transient and dissipate quickly, those that do not often become intolerable for the patient. The most common side effects from ET DBS are sensory paresthesias, dysarthria, and motor contractions. Sensory paresthesias are sensations such as numbness, burning, or tingling of the skin [17] and are thought to result from stimulation of the ventralis caudalis (Vc, or ventral posterior, VP) nucleus of the thalamus or the lemniscal fibers [18]. Approximately 10% of patients experience sustained paresthesias during programming [19], and it can be avoided by reducing stimulation voltage, moving the probe anterior, or using a higher contact on the DBS lead. Dysarthria affects 5-25% of patients [20-

22] and is thought to be caused by stimulation of the internal capsule (IC) or corticobulbar fibers, lateral to the DBS target for ET [23, 24]. While some patients can tolerate mild dysarthria in exchange for tremor control, dysarthria can be avoided with proper positioning of the DBS lead [17]. Motor contractions can also result from stimulation of the IC [25].

In this study, we utilize VTA modeling to investigate common side effects from thalamic DBS in 10 ET patients with well-positioned leads. We implemented the methodology presented in an accompanying study to measure the VTA overlaps with nuclei of interest to correlate stimulation settings to clinical outcome. We compare the ability of individualized and atlas-based VTA modeling systems to explain common side effects. This article presents our results and discusses limitations and the potential for individualized modeling to be used prospectively for surgical planning.

4.2. Materials and methods

Using the methods from Chapter 3, we sought to understand the most common side effects from thalamic DBS in ET patients with well-placed leads. Stimulation volumes were then calculated for clinically-efficacious and side effect-inducing stimulation settings and their overlaps with relevant anatomy were compared.

4.2.1 Patient Selection and Clinical Data

We retrospectively evaluated the VTAs of the same 10 ET patients who had successfully undergone unilateral left Vim (VLPv) DBS for advanced idiopathic ET (6 men, 4 women, age mean ± SD 66 ± 7 years, range 49-74 years) and whose leads were confirmed to be well-placed (see Chapter 3). We performed the study in

accordance with the policies of the Medical Institutional Review Board of the University of Michigan.

For VTA modeling, stimulation settings were selected from each patient's first stimulation programming session with a Neurologist (KLC) following the post-operative CT scan, 6-8 weeks post-DBS surgery. We recorded DBS settings on each contact (0-3) that controlled tremor without producing side-effects and stimulation settings on the same contacts that caused an explicitly noted side effect(s) (i.e., sustained sensory paresthesias, dysarthria, or speech issues).

4.2.2 Image Data Acquisition and Analysis and Thalamic Segmentation

Detailed methodology for image acquisition and analysis and thalamic segmentation can be found in Chapter 3.

4.2.3 VTA Analysis

The VTA is an estimate of the region(s) of the brain that fires action potentials under a given set of stimulation parameters [15]. We generated the VTAs for clinically efficacious and side effect-inducing stimulation settings, characterized their overlaps with relevant anatomy, and compared the performance of atlas-based and individualized VTA models in predicting side effects (sustained sensory paresthesias and dysarthria).

All simulations were performed on a custom-built computer with 8 processors and 48 GB memory (DEH Microsystems LLC, Cleveland, OH, USA) using BioPSE (Scientific Computing and Imaging Institute, University of Utah, Salt Lake City, UT).

4.2.3.1 VTA Generation

For each patient, atlas-based and individualized VTAs were generated individualized. The individualized VTA model followed the methodology presented in Chapter 3.

4.2.3.2 VTA Evaluation

For each stimulation setting, the overlap volumes between the VTA and the motor thalamus (VLPv, VLPd, VLa) sensory thalamus (VPM and VPL), and the internal capsule (IC, lateral to the thalamus) were recorded with the individualized and atlas-based models. Overall agreement in VTA volumes between the two models was assessed with a two-tailed paired t-test. Within models, VTAs at side-effect threshold voltages were compared to VTAs at voltages eliciting tremor control with paired t-tests to assess the overlap between VTAs and nuclei thought to cause side effects (i.e., sensory thalamus or IC). Between models, the ability of individualized or atlas-based models to predict the incidence of side-effects was assessed by comparing VTA volume overlaps in the sensory nucleus and internal capsule with paired t-tests. The ability of VTA modeling to predict dysarthria and other speech side effects was measured with Barnard's Exact test for each type of modeling (i.e., stimulation in the IC was treated as a binary variable). Barnard's Exact test is more appropriate than a Chi-Squared test or Fisher's Exact test because Fisher's Exact test requires two fixed margins (not applicable here) and the Chi-Squared test is less powerful when any of the cell values in a 2x2 table are less than 5 [26, 27].

4.2.4 Statistical Methods

Statistical analysis was performed using commercially available software: Excel (Microsoft Inc., Redmond, WA) and MATLAB (Mathworks, Natick, MA). For all

comparisons, statistical significance is defined at the $p = .05$ level. Sources of statistical variability in our data include quantization effects due to voxel representation intrinsic to MR imaging, motion artifacts in MR and CT imaging, and human error in measurement [28]. Data are displayed as mean ± SD except where otherwise noted.

4.3. Results

4.3.1 Clinical Outcome

All 10 patients had improved tremor following successful DBS surgery without sustained paresthesias or dysarthria.

4.3.2 VTA Analysis

During stimulation setting adjustment, patients typically experience transient paresthesias that dissipate quickly [17]. However, in some stimulation settings, the paresthesias become sustained and may be intolerable for the patient [3]. Sensory paresthesias are a common side-effect of thalamic VLPv (Vim) stimulation and are thought to be the result of stimulation in the VPL (Vc) [29]. Other common side-effects include dysarthria and tonic contractions, both thought to be caused by IC stimulation [17].

Paired t-tests show that there is no statistically significant difference between the sizes of VTAs generated by individualized and atlas-based modeling. The mean percentage difference between the size of individualized and atlas-based VTAs is 0.26% ± 22.37%.

Figure 4-1 shows four stimulation settings in one patient with individualized VTAs. The top row shows the difference between tremor control (Fig. 4-1A, 0.7 mm^3 stimulation) and sensory paresthesias (Fig. 4-1B, 5.11 mm^3) on the same contact. The bottom row shows another example of tremor control (contact 2) and sustained sensory paresthesias (contact 0), where contact 2 lies entirely within the VLPv and contact 0 is solidly within the sensory thalamus. Figure 4-2 shows an example of atlas-based and individualized VTA modeling predicting a VTA within the sensory thalamus, eliciting sensory paresthesias on contact 0. VTA models of two patients with dysarthria are shown in Figure 4-3. Atlas-based modeling (Figs. 4-3A and 4-3C) predicts no IC stimulation, while fully individualized modeling (Figs. 4-3B and 4-3D) predicts IC stimulation, shown in blue.

4.3.2.1 Within-Models Analysis

Results of within-methods analysis is provided in Table 4-1. Both methods predict significantly more sensory thalamus stimulation in VTAs eliciting sustained sensory paresthesias than in cases without side effects. The methods differ on whether there is more IC stimulation in VTAs eliciting dysarthria than in cases without side effects.

When stimulation is instead treated as a binary variable, individualized VTA modeling shows a statistically significant relationship between the presence of IC stimulation and dysarthria and other speech-related side effects (Barnard's Exact test, $p < 0.05$), whereas atlas-based VTA modeling does not (Barnard's Exact test, $p > 0.05$). Conversely, only atlas-based VTA modeling shows a statistically significant relationship between the presence of sensory thalamus stimulation and sustained sensory paresthesias (Barnard's Exact test, $p < 0.05$; individualized Barnard's Exact test, $p > 0.05$).

	Individualized	Atlas-Based
Sensory Thalamus stimulation with paresthesias: paired t-test (per contact)	**	**
Sensory Thalamus stimulation with paresthesias: two-sample t-test		
IC stimulation with dysarthria: paired t-test (per contact)	*	
IC stimulation with dysarthria: two-sample t-test		

Table 4-1. Summary of within-models statistical analysis. Key: $p < 0.01$ = **; $p < 0.05$ = *; blank indicates lack of statistical significance ($p > 0.05$).

4.3.2.2 Between-Models Analysis

There is no statistically significant difference in the volume of sensory thalamus stimulation during sustained side effects (two-tailed paired t-test, $p > 0.05$). There is significantly more IC stimulation during dysarthria in individualized modeling (~12.7 mm^3 vs. 0.44 mm^3; one-tailed paired t-test, $p < 0.05$)

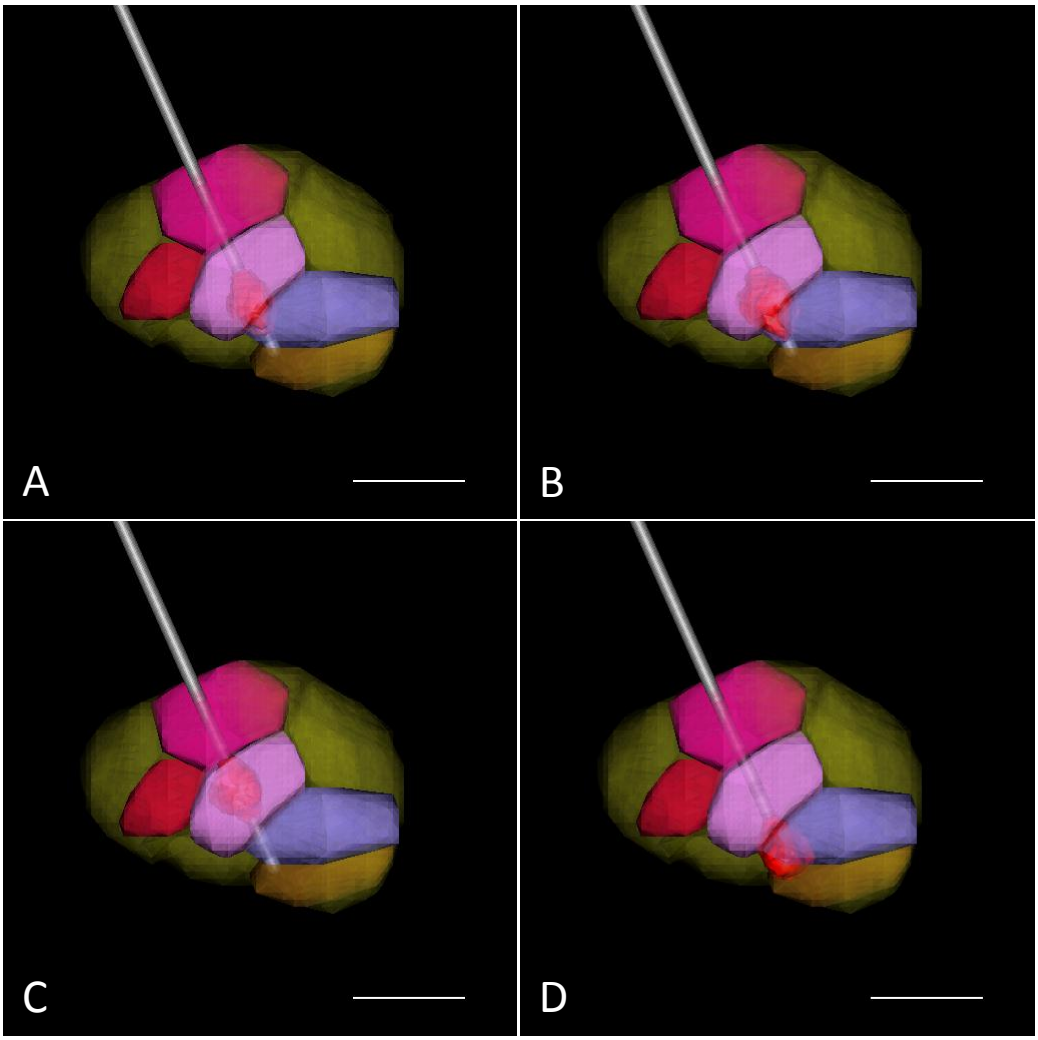

Figure 4-1. Comparison of Individualized VTAs on different contacts for the same patient. VTAs on different contacts induce different results in the same patient. (A) Tremor control on contact 1 (1.5 V). The VTA lies mostly within the motor thalamus, but there is small (0.7 mm^3) stimulation in the sensory thalamus. (B) Sustained sensory paresthesias on contact 1 (2.5 V). The VTA extends further into the sensory thalamus (5.11 mm^3). (C) Excellent tremor control on contact 2 (1.5 V). The VTA does not extend into the sensory thalamus. (D) On contact 0 (2 V), sustained paresthesias from sensory thalamus stimulation (18.25 mm^3). Scale bars represent 10 mm. (key: crimson = VLa, magenta = VLPd, pink = VLPv, purple = VPL, brown = VPM)

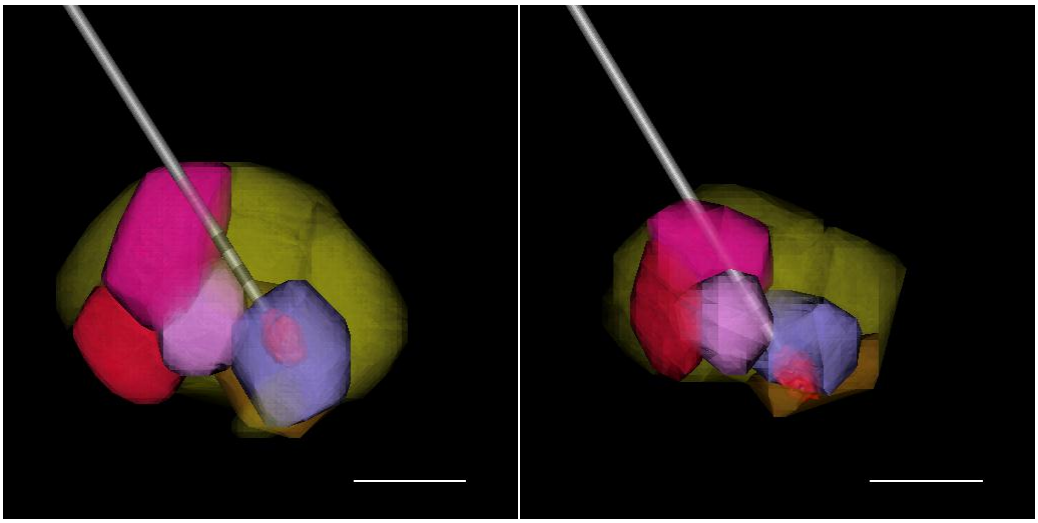

Figure 4-2. Comparison of Atlas-based and Individualized VTA modeling during sustained sensory paresthesias. Atlas-based (left) and individualized (right) VTA models both predict sensory thalamus stimulation in a patient experiencing sustained paresthesias on contact 0 (1 V). Scale bars represent 10 mm. (key: crimson = VLa, magenta = VLPd, pink = VLPv, purple = VPL, brown = VPM)

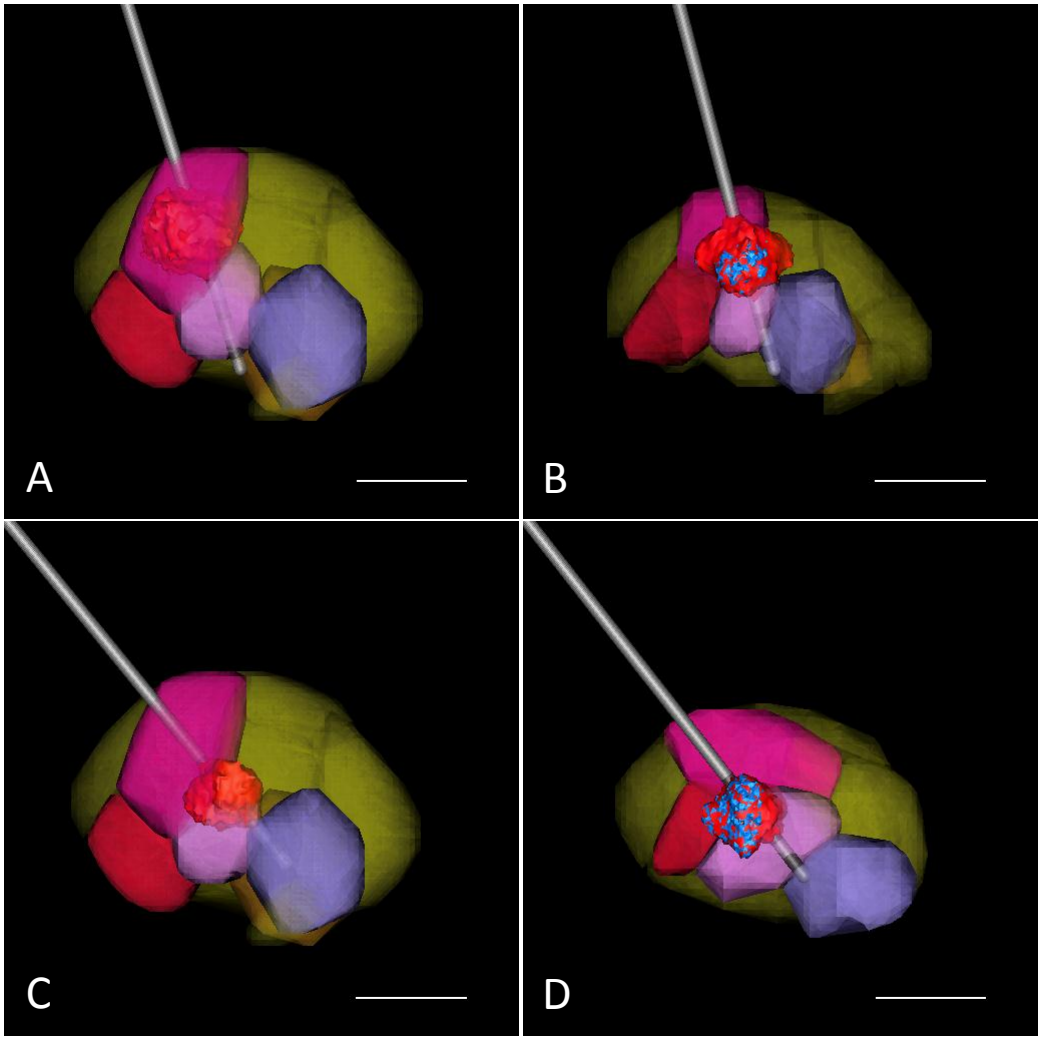

Figure 4-3. Comparison of Atlas-based and Individualized VTA modeling during dysarthria. (A) Atlas-based modeling shows a VTA that elicited dysarthria (Contact 3, 2.5 V) that lies entirely within the motor thalamus, with no stimulation in the IC. (B) Individualized modeling shows the VTA of the same setting with stimulation in the IC (indicated in blue, 2.09 mm^3). (C) Atlas-based modeling shows a VTA that elicited dysarthria (Contact 2, 2.5V) that lies mostly within the motor thalamus, with no stimulation in the IC. (D) Individualized modeling shows the VTA of the same setting with stimulation in the IC (indicated in blue, 33.43 mm^3). Scale bars represent 10 mm. (key: crimson = VLa, magenta = VLPd, pink = VLPv, purple = VPL, brown = VPM)

4.4. Discussion

In this study, we utilized an individualized VTA model to investigate side effects from thalamic DBS for ET. We conducted this investigation in two parallel tracks to compare the performance of atlas-based and individualized VTA modeling by assessing each model's ability to correlate VTA location with patient outcomes across 10 ET DBS patients.

4.4.1 Previous Work

Prior computational investigations of ET DBS assumed that the division between the motor and sensory nuclei modulates the incidence of sensory paresthesias. However, no prior study implemented an individualized approach, instead co-registering patient data to brain atlases or utilizing common brain spaces to draw conclusions across patients. The earliest of these studies estimated the spatial extent of activation in thalamic DBS with a basic amplitude-distance relationship, concluding that placing the DBS electrode in the posterior portion of the VLPv/Vim can cause stimulation of the VPL/Vc, and therefore sensory paresthesias, even at low voltages [30]. Pouratian et al. [31] analyzed the connectivity between the most efficacious DBS contact for tremor control and prefrontal, premotor, and primary motor cortical target masks using probabilistic diffusion tractography [32] within Montreal Neurological Institute (MNI) brain space. It was determined that the most efficacious DBS contact for tremor control typically lies in an area with high likelihood of connectivity with the premotor and supplementary motor cortices. A recent study investigated the potential for directional DBS leads to modulate neuronal pathways with a finite-element electric field model of rodent Vc/Vim afferent and efferent neurons, though this study took a more simplified approach by assuming an isotropic homogeneous tissue

conductivity and utilized atlas nuclei warping instead of segmenting individually [29].

4.4.2 VTA Analysis

While there is no statistically significant difference in VTA sizes between models (paired t-test, $p > 0.05$), the standard deviation in percentage difference between models is large (~22%), indicating high variability. This finding may be explained by electrode positioning and surrounding tissue conductivity. The differences in electrode placement are attributable to the non-linear warping algorithm employed by Cicerone [33], which places each patient's DBS lead in an appropriate position within the atlas thalamus [34]. Cicerone's positioning of the DBS lead in the atlas thalamus may result in the active contact being placed in an area with different tissue conductivity compared to individualized modeling. Therefore, VTA sizes may vary between models.

Our results suggest that there are differences in the predictive abilities of individualized and atlas-based VTA modeling. Individualized modeling can predict IC stimulation that results in dysarthria, while atlas-based modeling does not. Atlas-based modeling attributes the incidence of sustained sensory paresthesias to sensory thalamus stimulation, but individualized modeling suggests that the internal capsule may be responsible for paresthesias, especially those observed on proximal contacts (2 and 3).

4.2.1 Dysarthria

There are two major advantages to investigating dysarthria. First, dysarthria is an observable condition, unlike sustained sensory paresthesias. Second, dysarthria

results from IC stimulation, which is not dependent upon the accuracy of thalamic segmentation. However, IC stimulation is generally rare in atlas-based modeling. Cicerone's electrode placement is generally too medial for a VTA to stimulate the IC compared to individualized modeling. Ultimately, individualized modeling places the electrode where it really is in the patient, which is often close to the lateral border of the thalamus. Individualized modeling is superior to atlas-based modeling in both within- and between-models analyses in the ability to predict dysarthria from IC stimulation.

4.2.2 Sustained Sensory Paresthesias

As expected, sensory thalamus stimulation is relatively uncommon in patients with well-placed leads. Nevertheless, most patients experienced sustained sensory paresthesias on proximal contacts (2 and 3), which are anterodorsal to the sensory thalamus in well-positioned leads, regardless of thalamic segmentation results. Of the 23 settings that caused sustained sensory paresthesias, 8 occurred on contact 0, 7 on contact 1, 5 on contact 2, and 3 on contact 3; therefore, nearly a third of sustained sensory paresthesias in this study cannot be attributed to sensory thalamus stimulation. An analysis between models reveals no significant difference in the volume of sensory thalamus stimulated, suggesting good agreement between models, and in both models, there is more sensory thalamus stimulation at paresthesia thresholds in a paired analysis on each contact. However, sensory thalamus stimulation is not greater overall when comparing tremor control to sensory paresthesias. This result suggests three things: (1) that some sensory thalamus stimulation does not necessarily elicit sustained paresthesias, (2) that the k-means algorithm is not correctly predicting the boundaries of the thalamic nuclei and (3) that sensory paresthesias may result from stimulation outside of the sensory thalamus. Lastly, sustained paresthesias are not an observable side effect, unlike

dysarthria. Given that DBS programming does not occur in a randomized order, there is reason to believe that patients may over-report the incidence of sustained sensory paresthesias or mistake a mild motor contraction for a sensory paresthesia. We considered the possibility that IC stimulation causes some paresthesias. In individualized modeling, 76% of paresthesias not attributable to sensory thalamus stimulation may result from IC stimulation (compared to atlas-based modeling, 30%). Assuming this alternative explanation for patient-reported sensory paresthesias, individualized modeling predicts 87% of sensory paresthesias while atlas-based modeling only predicts 70%.

4.4.3 Limitations and Future Directions

The interpretation of our results is subject to several limitations. First, our sample size (N = 10) is relatively small; we restricted this investigation to include only patients without co-morbid conditions and with well-placed leads. Though our sample size is larger than most other VTA studies, it is still likely insufficient for robust statistical analysis. Additionally, DTI is low-resolution, and VTA analysis and thalamic segmentation rely on resampling the DTI images; there is expected error from DTI resampling, especially at tissue boundaries. Next, this study was restricted to monopolar stimulation settings at a frequency of 130Hz and pw of 60 μs; different frequencies and pulse widths are subject to different axonal activation functions within the VTA model. The neurologist's (KLC) DBS programming protocol is standardized but not randomized, which may result in false positive side effect reporting. Our analysis of sustained sensory paresthesias is limited by the thalamic segmentation method used. Though more robust methods have been reported in the literature [35], the k-means algorithm was a convenient choice for the retrospective data available. While the analysis of IC stimulation is not limited by thalamic segmentation, it remains limited by the accuracy of parcellation.

Further, VTA analysis is complicated by the fact that characterizing stimulation overlap is inherently difficult. Even if thalamic segmentation were completely correct, the exact locations within certain nuclei that can produce side effects or tremor control when stimulated are not known. As a result, whether to treat VTA overlap as a volume measurement or a binary variable for analysis is unclear. While atlas-based modeling theoretically has the advantage of determining common locations for tremor control or side effects, our data suggests that the shortcomings of atlas-based modeling may preclude such an investigation.

We plan to implement individualized modeling in a prospective analysis of ET patients undergoing DBS. Given the demonstrated ability of individualized modeling to correlate IC stimulation with dysarthria, we will evaluate this technique's ability to prospectively predict side-effects based on electrode placement and VTA stimulation overlaps.

4.5. Conclusions

A comparison of individualized VTA modeling to existing atlas-based VTA modeling suggests that individualized VTA modeling better explains the incidence of side effects, especially dysarthria from IC stimulation. A prospective study is planned for further investigation (see Chapter 5).

4.6. References

1. Benabid, A.L., et al., Chronic electrical stimulation of the ventralis intermedius nucleus of the thalamus as a treatment of movement disorders. J Neurosurg, 1996. **84**(2): p. 203-14.

2. Koller, W., et al., High-frequency unilateral thalamic stimulation in the treatment of essential and parkinsonian tremor. Ann Neurol, 1997. **42**(3): p. 292-9.

3. Koller, W.C., et al., Long-term safety and efficacy of unilateral deep brain stimulation of the thalamus in essential tremor. Mov Disord, 2001. **16**(3): p. 464-8.

4. Kumar, R., et al., Long-term follow-up of thalamic deep brain stimulation for essential and parkinsonian tremor. Neurology, 2003. **61**(11): p. 1601-4.

5. Klein, J.C., et al., The tremor network targeted by successful VIM deep brain stimulation in humans. Neurology, 2012. **78**(11): p. 787-95.

6. Vitek, J.L., Mechanisms of deep brain stimulation: excitation or inhibition. Mov Disord, 2002. **17 Suppl 3**: p. S69-72.

7. McIntyre, C.C., et al., Uncovering the mechanism(s) of action of deep brain stimulation: activation, inhibition, or both. Clin Neurophysiol, 2004. **115**(6): p. 1239-48.

8. Montgomery, E.B., Jr. and J.T. Gale, Mechanisms of action of deep brain stimulation(DBS). Neurosci Biobehav Rev, 2008. **32**(3): p. 388-407.

9. Butson, C.R., et al., Predicting the effects of deep brain stimulation with diffusion tensor based electric field models. Med Image Comput Comput Assist Interv, 2006. **9**(Pt 2): p. 429-37.

10. Miocinovic, S., et al., Computational analysis of subthalamic nucleus and lenticular fasciculus activation during therapeutic deep brain stimulation. J Neurophysiol, 2006. **96**(3): p. 1569-80.

11. Chaturvedi, A., et al., Subthalamic nucleus deep brain stimulation: accurate axonal threshold prediction with diffusion tensor based electric field models. Conf Proc IEEE Eng Med Biol Soc, 2006. **1**: p. 1240-3.

12. Butson, C.R., et al., Patient-specific analysis of the volume of tissue activated during deep brain stimulation. Neuroimage, 2007. **34**(2): p. 661-70.

13. Butson, C.R. and C.C. McIntyre, Current steering to control the volume of tissue activated during deep brain stimulation. Brain Stimul, 2008. **1**(1): p. 7-15.

14. Maks, C.B., et al., Deep brain stimulation activation volumes and their association with neurophysiological mapping and therapeutic outcomes. J Neurol Neurosurg Psychiatry, 2009. **80**(6): p. 659-66.

15. Chaturvedi, A., et al., Patient-specific models of deep brain stimulation: influence of field model complexity on neural activation predictions. Brain Stimul, 2010. **3**(2): p. 65-7.

16. Butson, C.R., et al., Probabilistic analysis of activation volumes generated during deep brain stimulation. Neuroimage, 2011. **54**(3): p. 2096-104.

17. Marks, W.J., Jr., Deep Brain Stimulation Management. 2011, New York: Cambridge University Press.

18. Deuschl, G., et al., Deep brain stimulation: postoperative issues. Mov Disord, 2006. **21 Suppl 14**: p. S219-37.

19. Alesch, F., et al., Stimulation of the ventral intermediate thalamic nucleus in tremor dominated Parkinson's disease and essential tremor. Acta Neurochir (Wien), 1995. **136**(1-2): p. 75-81.

20. Albanese, A., et al., Long-term ventralis intermedius thalamic stimulation for parkinsonian tremor. Italian Registry for Neuromodulation in Movement Disorders. Adv Neurol, 1999. **80**: p. 631-4.

21. Kumar, K., M. Kelly, and C. Toth, Deep brain stimulation of the ventral intermediate nucleus of the thalamus for control of tremors in Parkinson's disease and essential tremor. Stereotact Funct Neurosurg, 1999. **72**(1): p. 47-61.

22. Limousin, P., et al., Multicentre European study of thalamic stimulation in parkinsonian and essential tremor. Journal of Neurology, Neurosurgery & Psychiatry, 1999. **66**(3): p. 289-296.

23. Krack, P., et al., Postoperative management of subthalamic nucleus stimulation for Parkinson's disease. Mov Disord, 2002. **17 Suppl 3**: p. S188-97.

24. Tamma, F., et al., Anatomo-clinical correlation of intraoperative stimulation-induced side-effects during HF-DBS of the subthalamic nucleus. Neurol Sci, 2002. **23 Suppl 2**: p. S109-10.

25. Ashby, P., et al., Neurophysiological effects of stimulation through electrodes in the human subthalamic nucleus. Brain, 1999. **122 (Pt 10)**: p. 1919-31.

26. Barnard, G., Significance tests for 2× 2 tables. Biometrika, 1947: p. 123-138.

27. Mehta, C.R. and P. Senchaudhuri, Conditional versus unconditional exact tests for comparing two binomials. Cytel Software corporation, 2003. **675**.

28. Patil, P.G., et al., The anatomical and electrophysiological subthalamic nucleus visualized by 3-T magnetic resonance imaging. Neurosurgery, 2012. **71**(6): p. 1089-95; discussion 1095.

29. Keane, M., et al., Improved spatial targeting with directionally segmented deep brain stimulation leads for treating essential tremor. J Neural Eng, 2012. **9**(4): p. 046005.

30. Kuncel, A.M., S.E. Cooper, and W.M. Grill, A method to estimate the spatial extent of activation in thalamic deep brain stimulation. Clin Neurophysiol, 2008. **119**(9): p. 2148-58.

31. Pouratian, N., et al., Multi-institutional evaluation of deep brain stimulation targeting using probabilistic connectivity-based thalamic segmentation. J Neurosurg, 2011. **115**(5): p. 995-1004.

32. Behrens, T.E., et al., Non-invasive mapping of connections between human thalamus and cortex using diffusion imaging. Nat Neurosci, 2003. **6**(7): p. 750-7.

33. Christensen, G.E., S.C. Joshi, and M.I. Miller, Volumetric transformation of brain anatomy. IEEE Trans Med Imaging, 1997. **16**(6): p. 864-77.

34. Miocinovic, S., et al., Cicerone: stereotactic neurophysiological recording and deep brain stimulation electrode placement software system. Acta Neurochir Suppl, 2007. **97**(Pt 2): p. 561-7.

35. Deoni, S.C., et al., Segmentation of thalamic nuclei using a modified k-means clustering algorithm and high-resolution quantitative magnetic resonance imaging at 1.5 T. Neuroimage, 2007. **34**(1): p. 117-26.

Chapter 5

Conclusions and Future Directions

5.1 Conclusions

Optimized targeting is of considerable interest to neurosurgeons and researchers aiming to improve the safety and efficacy of DBS surgery. The work presented in this dissertation advances the knowledge of proper DBS surgery targeting for movement disorders. The results in Chapter 2 resolve a longstanding debate in the DBS field by establishing a superior indirect targeting technique for STN DBS with a validated imaging protocol. Neurosurgeons relying on indirect targeting for STN DBS should routinely use the RN-based technique over the MCP-based technique due to its greater accuracy and precision. Chapter 3 presents an individualized targeting and tissue activation modeling system for thalamic Vim DBS. The k-means clustering algorithm presented in Chapter 3 is robust and capable of accurately segmenting the thalamus into its functionally-distinct nuclei. Because preliminary results in Chapter 3 indicate that individualized VTA modeling may be superior to atlas-based modeling, Chapter 4 compares the performance of individualized and atlas-based VTA modeling by applying them to the study of common side effects of thalamic DBS. Results demonstrate that individualized VTA modeling is superior to atlas-based modeling in the ability to predict certain side effects. The individualized VTA model for thalamic VLPv

(Vim) DBS is currently the most patient-customized DBS model available and is adaptable to other DBS targets. The development of individualized DBS targeting and modeling is a substantial step towards optimized DBS targeting, but additional work is required to further validate the model and test it in a prospective setting.

5.2 Future Directions

5.2.1 Current Techniques

Atlas-based modeling has the theoretical advantage of allowing for easy comparison across subjects. By modeling VTAs in a single brain, researchers may find specific targets (e.g., dorsal STN for PD tremor [1-5]) that produce common clinical effects across patients. This can be accomplished by calculating the intersection of VTAs across a cohort experiencing the same clinical effect. However, Chapters 3 and 4 demonstrated that atlas-based VTA modeling may position the probe in an inappropriate location, which would preclude an accurate analysis of common clinical targets. A shift towards individualized modeling is justified according to the results presented in this dissertation, and could assist in proper DBS targeting for movement disorders.

5.2.2 Changes Required for Implementation of Proposed Methods

Implementation of thalamic segmentation-based DBS targeting would ideally involve rigorous validation beyond the results presented in Chapter 3. As discussed in Chapter 3, there is no in-vivo gold standard for validating the results of the segmentation algorithm. There are two options for validation. The first is to superimpose the results of thalamic segmentation onto patient-specific fiber tractography and probabilistic connectivity maps with the methodology presented by Pouratian et al. [6]. A significant drawback to this proposal is that fiber

tractography and probabilistic connectivity rely on DTI, and therefore suffer from the same limitations as our segmentation algorithm. Improved DTI resolution may overcome this drawback. Alternatively, a long-term validation study could be attempted with post-mortem data. By conducting histological staining as presented by Morel et al. [7] to compare the results of thalamic segmentation with histological boundaries, the segmentation algorithm could potentially be validated. The major drawbacks to this proposal are the significant time investment and potentially small sample size.

Further, implementation of thalamic segmentation-based DBS targeting would require several changes to existing technology (StealthStation Surgical Navigation System, Medtronic, Minneapolis, MN). The StealthStation system currently orients an anatomic MR image along the intercommissural and interhemispheric planes with user guidance. An anatomic atlas (Schaltenbrand and Wahren [8]) is overlaid onto the image, and the neurosurgeon manually positions and scales the atlas to match the MR image. Once the neurosurgeon feels that the atlas is properly scaled, the StealthStation provides target coordinates, taking into account the length of the AC-PC line. This method is limited by its simplicity and is prone to error. Unlike commercial image coregistration programs (e.g. Analyze 11.0, AnalyzeDirect, Overland Park, KS) with automated coregistration algorithms [9], current stereotactic targeting relies on a neurosurgeon to properly scale an atlas. However, without the assistance of a built-in coregistration algorithm, this procedure is imprecise and potentially inaccurate.

In order to implement thalamic segmentation, three additional data sets would be necessary: the coordinates of the thalamus (manually parcellated prior to surgery, which takes approximately 30 minutes for an experienced user), corresponding

diffusion tensors for each voxel in the thalamus, and the centroids of the atlas thalamic nuclei. The coordinates of the thalamus can be exported by Analyze 11.0, and corresponding diffusion tensors can be exported by Matlab (Mathworks, Natick, MA). A more powerful system would require the processing power to automatically calculate diffusion tensors from DTI images and crop thalamic tensors from the loaded parcellated thalamus. The coordinates of atlas thalamic nuclei centroids would need to be calculated only once, and stored as a feature of the StealthStation. Initial centroid coordinates of thalamic nuclei could be derived from the coordinates reported by Deoni et al. [10], but would require a coordinate transformation to scale them appropriately for each patient. Neurosurgeons would continue to manually scale the atlas to match the patient brain for two reasons. First, atlas scaling would give the standard targeting coordinates for a prospective study. Second, the transformation matrix from atlas scaling could be used to calculate appropriate initial centroids for the k-means thalamic segmentation algorithm via a rigid coordinate transformation.

Once the initial centroid coordinates are transformed into patient space, the algorithm would take less than 10 minutes to run (provided the specifications of the intraoperative machine are similar to the computers described in Chapters 3 and 4). The algorithm is capable of outputting the coordinates of the centroid of any nucleus and all the voxel coordinates that lie within a nucleus. The Y and Z coordinates of the VLPv centroid could be used for initial DBS targeting; the X coordinate of the VLPv centroid is generally not used for DBS targeting due to the somatotopic organization of the thalamus [11]. The active contact is situated approximately 1.8 medial to the VLPv centroid, according to our data. Contact 2 on the 3387 Medtronic probe would most likely be used for targeting the location recommended by the segmentation algorithm.

The coordinates of the DBS target could be refined with VTA-based targeting and parameter selection. Implementation of VTA-based stimulation parameter selection would be more complicated, and would require more computationally powerful equipment than what is currently used. Further, an intraoperative VTA model would require that there be no fibrous capsule assumption. Generally, good tremor control is found at stimulation voltages less than 3V where the VTA lies entirely within the motor thalamus (preferably VLPv, though sometimes VLPd and VLa). Overlap with the sensory thalamus (VPL, VPM) must be avoided as well as overlap with the IC, which was demonstrated in Chapter 4 to reliably indicate the presence of dysarthria.

5.2.3 Benefits and Trade-Offs of Proposed Methods

The major trade-off with more complex targeting and modeling for DBS surgical planning is time. The current system is straightforward to operate and does not require a significant time investment; neurosurgeons are able to determine a target in a matter of minutes. Considering the high percentage of successful surgeries, the current system works well enough for clinical benefit. However, improved targeting has two main benefits: 1) fewer surgical tracks and 2) lower voltage to stimulate the correct spot, extending battery life and minimizing the incidence of side effects. Specifically, given that some patients tolerate some dysarthria in exchange for tremor control [12], there is clinical interest in being able to properly target to avoid dysarthria. Modeling and targeting could take place weeks before surgery, or as soon as pre-operative MR and DT imaging is completed.

5.2.4 Prospective Study

We plan to conduct a prospective consecutive study on ET patients in two parts order to directly test the conclusions of this dissertation: thalamic segmentation-based targeting and preoperative side-effect prediction. ET Patients will be evaluated per DBS Pathway guidelines at the University of Michigan, and comorbid conditions will be noted. 10 ET patients with limited or no comorbid conditions will be selected to participate in this study. We will obtain institutional review board approval from the University of Michigan prior to selecting patients.

First, the viability of thalamic segmentation for DBS targeting will be tested. Thalamic segmentation will be performed preoperatively and targeting will be informed by the position of the centroid of the VLPv nucleus. The Y and Z coordinates of the VLPv centroid will be the DBS target for contact 2 of the 3387 probe, while the X contact will be 1.8 mm medial to the X coordinate of the VLPv centroid. This trajectory will be compared to the standard thalamic DBS targeting protocol (see Chapter 1 for details; the distal tip of the electrode is placed according to atlas relationships, and contact 1 is the most common final active contact). The neurosurgeon will attempt two surgical trajectories in a randomized order with the standard and segmentation-based target coordinates. Tremor control—measured quantitatively with an accelerometer—will be compared for the two trajectories. The trajectory that reduces tremor the most (without any side simultaneous side effects) will be considered superior. If both trajectories effectively control tremor, the trajectory without side effects at the lowest voltage will be deemed the superior trajectory. It would be unsafe to proceed with each trajectory as though it were being independently evaluated (i.e., with multiple passes around the initial trajectory) due to the increased risk of intracranial hemorrhage [13]. As discussed in Chapter 2, simply calculating the distance

between a target coordinate and the final active contact as a way to determine optimal targeting is improper, as the position of the final active contact is ultimately determined by whichever targeting protocol is used.

Therefore, for the second part of the study, VTA overlaps with relevant nuclei (i.e., motor thalamus, sensory thalamus, IC) will be measured preoperatively for the target coordinates. For standard thalamic DBS targeting and segmentation-based thalamic DBS targeting, contacts 1 and 2 would be used, respectively. The VTAs will be generated for each targeting method for a monopolar stimulation configuration (frequency 130 Hz, pulse width 60 μs) at a range of voltages (0.5-5 V at 0.5 V increments). The incidence of sustained sensory paresthesias and dysarthria will be predicted prior to surgery with the intraoperative individualized VTA model, and intraoperative side-effects will be noted and compared against those predictions during randomized stimulation parameter testing.

This intraoperative prospective study would help to overcome the limitations of the retrospective data used in Chapters 3 and 4. However, an inherent difficulty of this study is the lack of statistical power; sample size is likely to remain low ($N \leq 10$). With improvements in imaging protocols, thalamic segmentation and VTA modeling will become refined. Ultimately, the goal is to understand how VTA modeling can predict good tremor control and avoid side effects, and further work will involve correlating VTA size and position to tremor frequency.

5.3 References

1. Hamel, W., et al., Deep brain stimulation of the subthalamic nucleus in Parkinson's disease: evaluation of active electrode contacts. Journal of Neurology, Neurosurgery & Psychiatry, 2003. **74**(8): p. 1036-1046.

2. Lanotte, M.M., et al., Deep brain stimulation of the subthalamic nucleus: anatomical, neurophysiological, and outcome correlations with the effects of stimulation. Journal of Neurology, Neurosurgery & Psychiatry, 2002. **72**(1): p. 53-58.

3. Saint-Cyr, J.A., et al., Localization of clinically effective stimulating electrodes in the human subthalamic nucleus on magnetic resonance imaging. Journal of neurosurgery, 2002. **97**(5): p. 1152-1166.

4. Yelnik, J., et al., Localization of stimulating electrodes in patients with Parkinson disease by using a three-dimensional atlas-magnetic resonance imaging coregistration method. Journal of Neurosurgery, 2003. **99**(1): p. 89-99.

5. Butson, C.R., et al., Patient-specific analysis of the volume of tissue activated during deep brain stimulation. Neuroimage, 2007. **34**(2): p. 661-70.

6. Pouratian, N., et al., Multi-institutional evaluation of deep brain stimulation targeting using probabilistic connectivity-based thalamic segmentation. J Neurosurg, 2011. **115**(5): p. 995-1004.

7. Morel, A., M. Magnin, and D. Jeanmonod, Multiarchitectonic and Stereotactic Atlas of the Human Thalamus. The Journal of Comparative Neurology, 1997. **3877**: p. 588-630.

8. Schaltenbrand, G. and W. Wahren, Atlas for Stereotaxy of the Human Brain. 1977, Stuttgart: Thieme.

9. Studholme, C., D.J. Hawkes, and D.L. Hill. Normalized entropy measure for multimodality image alignment. 1998.

10. Deoni, S.C., et al., Segmentation of thalamic nuclei using a modified k-means clustering algorithm and high-resolution quantitative magnetic resonance imaging at 1.5 T. Neuroimage, 2007. **34**(1): p. 117-26.

11. Tasker, R.R., L.W. Organ, and P.A. Hawrylyshyn, The thalamus and midbrain of man: a physiological atlas using electrical stimulation. 1982: C.C. Thomas.

12. Marks, W.J., Jr., Deep Brain Stimulation Management. 2011, New York: Cambridge University Press.

13. Benabid, A.L., Deep brain stimulation for Parkinson's disease. Curr Opin Neurobiol, 2003. **13**(6): p. 696-706.